Faculty of Electrical Engineering and Information Technology
Ruhr-University Bochum, Germany

Diploma Thesis

Atomistic Modeling of an experimental GaAs/InGaAs Quantum Dot Molecule using NEMO 3-D

Yui-Hong "Matthias" Tan

In Partial Fulfillment of the Requirements for the Degree

Diplom-Ingenieur (Dipl.-Ing.)

Advisors

Prof. Dr. Gerhard Klimeck, Purdue University

Prof. Dr. Ulrich Kunze, Ruhr-University Bochum

September 2010

Purdue University

West Lafayette, Indiana, USA

I hereby affirm that I composed this work myself and did not use any but the denoted resources.

West Lafayette, September 2010

This thesis is dedicated to my parents

ACKNOWLEDGEMENTS

TABLE OF CONTENTS

LIST OF TABLES

Table   Page

LIST OF FIGURES

ABSTRACT

Over the last decade, the ongoing improvement of nanofabrication technologies has opened the way for novel nano-devices and semiconductor structures with sizes of a few tens of nanometers. One realization of such semiconductor devices can be found in the application of quantum dots. Quantum dots are characterized by their ability to confine carriers in all three spatial dimensions on a nanometer scale.

Quantum dots are often referred to as "artificial atoms" with discrete atomic-like energy states resulting from quantum mechanical carrier confinement. Quantum dot structures therefore offer us the opportunity to study quantum mechanical effects of atomic systems on a nanometer scale. From an application point of view quantum dots find use in a wide spectrum of areas ranging from lasers, photo detectors and lighting to medical imaging. Quantum dot structures are also intensely studied as promising candidates in the realization of quantum computing applications.

The main work of this thesis comprises a theoretical study of an experimentally investigated InGaAs quantum dot molecule. Using NEMO-3D to perform atomistic electronic structure calculations on a multi-million atom scale, we quantitatively reproduce and analyze an experimentally measured excitonic spectrum of the examined InGaAs quantum dot molecule. Furthermore, we highlight and discuss the importance of piezoelectric effects in achieving agreement of our simulations results with the experimental excitonic spectrum.

In the first chapters, we present a short introduction to quantum dots and the Quantum Confined Stark Effect, illustrated by simulations of single and vertically stacked quantum dot structures. The subsequent chapters will continue with the study on the InGaAs quantum dot molecule and focus our discussion on the experimental excitonic spectrum.

1. NEMO-3D

The simulations of the quantum dot structures in this thesis were carried out using the 3-D NanoElectronic Modeling (NEMO-3D) tool. The software enables the atomistic simulation and computation of strain and electronic structure in multi-million atoms nanostructures. NEMO 3-D can handle strain and electronic structure calculations consisting of more than 64 and 52 million atoms, corresponding to nanostructures of $(110nm)^3$ and $(101nm)^3$, respectively. [50]

Applications of NEMO 3-D in realistically sized nanostructures include self-assembled single quantum dots, stacked quantum dot systems, SiGe quantum wells, SiGe nanowires and nanocrystals. [14]

NEMO-3D is the successor of the 1D Nanoelectronic modeling tool (NEMO) and was developed by Professor Dr. Gerhard Klimeck on Linux clusters at the NASA Jet Propulsion Laboratory. NEMO 3-D was released in 2003 and is until now used in simulation tools on nanoHUB.org reaching out to and impacting the work of thousands of users. NEMO 3-D runs on serial and parallel platforms, local cluster computers, as well as the National Science Foundation Teragrid. For a detailed view on the development of NEMO-3D the reader may be referred to the following publications. [13, 14, 15]

In the following, I would like to outline the underlying physical models and concepts used in NEMO 3-D and subsequently continue with a sample case study of a single quantum dot to illustrate the general simulation flow of NEMO 3-D.

As modern nanoelectronic structures reach size domains of few tens of nanometers, the quantum mechanical nature of charge carriers becomes an important factor in modeling and determining nanoelectronic device properties. The atomic granularity of materials in these small regimes cannot be neglected and has to be considered to accurately model latest nanoelectronic devices.

To address the issues of pronounced quantum mechanical effects and atomic granularity, atomistic approaches therefore seem favorable in simulating electronic band structures in realistically sized nanoelectronic devices. Atomistic models aim to incorporate the electronic wave function of each individual atom.

The electronic band structure calculation in NEMO 3-D is based on a twenty band sp^3d^5s* nearest neighbor tight-binding model, which includes spin. Choosing the tight-binding model allows electronic structure simulation in atomistic resolution and is suitable to model finite device sizes, alloy disorder or heterointerfaces.

In the tight-binding formalism a basis is defined from a selection of atomic orbitals (e.g. s, p, and d) centered on each atom of the crystal, which create a single electron Hamiltonian. The Hamiltonian represents the electronic properties of the bulk material. Interactions between nearest neighbor atoms and between different orbitals within an atom are included by using empirical fitting parameters. Fitting parameters entering the electronic band structure calculation must be obtained or adjusted for each constituent material and bond type and verified against experimental data.

The need for empirical fitting parameters results in the major drawback of the tight-binding model and still continues to raise questions within the community about the fundamental applicability of tight-binding. Although tight binding requires empirical fitting, its advantages over comparable methods made tight binding the appropriate choice in the development of NEMO 3-D. For example, non-atomistic continuum methods such as effective mass or k_*p typically fail to capture the atomic granularity of materials inherent in the tight binding model.

Non-atomistic approaches do not model each atom individually in the structure, but rather approximate the underlying structure based on a continuous, jelly-type view of matter. This simplified description of matter makes non-atomistic models not well suited to address interface or disorder effects in nano-scale regimes.

Alternative atomistic approaches like pseudopotentials use plane waves as a fundamental basis choice. But with realistic nanostructures containing high-frequency features arising from alloy disorder or heterointerfaces, the basis needs to be adjusted each time for every different device. Besides the complex adjustment procedure, the numerical implementation of pseudopotential calculations is computationally more challenging as compared to tight binding.

To address the issue of empirical fitting in tight binding and take advantage of the model's full potential, the NEMO team spent significant effort to successfully expand and document the tight-binding capabilities. [40,42,43,44,45] Using tight binding, NEMO was able, for example, to early match experimentally obtained current-voltage curves of resonant tunneling diodes that could not be modeled by either effective mass or pseudopotential methods [13].

Strain plays an important role in nano-devices and its effects have to be taken into account to achieve accurate and realistic modeling in the nano-scale regime. In quantum dot structures, strain arises due to the lattice mismatch between the quantum dot and substrate material. For example, the difference in lattice constants in a typical InAs/GaAs system is on the order of 7% [13]. The effects of strain will be dealt with in more detail in the following chapters.

NEMO 3-D is capable of computing strain fields using an atomistic valence force field (VFF) method with the Keating potential [13]. In this model, the total elastic energy of the structure is obtained as a sum of bond-stretching and bond-bending contributions from each atom. The total elastic energy is then minimized to find the equilibrium atomic positions of each atom. To illustrate the program flow of NEMO 3-D, a typical simulation of a single quantum dot is presented. The general geometry of the structure is depicted in Figure 1. [14]
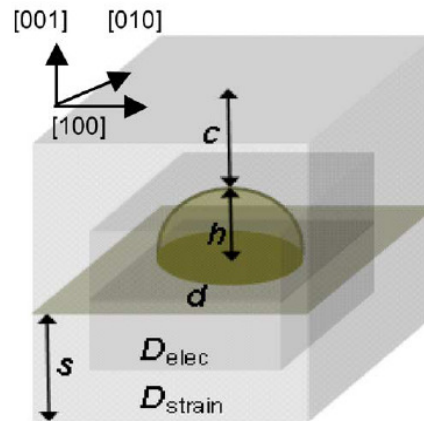
Figure 1.1:   Sample single quantum dot structure as implemented in NEMO 3-D, [14]

The structure consists of a single dome-shaped InAs quantum dot, which is embedded in a GaAs substrate. The dot has a diameter of 11.3nm and height of 5.65nm and is placed on a wetting layer of 0.6nm thickness. The electronic structure calculation is carried out in the small box D_{elec}, which contains around 0.3 million atoms. The strain domain D_{strain}, which contains around 3 million atoms, is chosen to be larger to sufficiently capture long-ranging strain fields. The calculation in the electronic box assumes closed boundary conditions whereas the strain domain assumes open boundary conditions in the lateral dimensions and open boundary conditions on the top surface.

   The NEMO 3-D simulation flow consists of four main components. [13] In the first part of the simulation, the geometry is constructed in atomistic detail. In this process, each atom is assigned a three single-precision number to identify its position within the structure. Furthermore, the geometry constructor saves the atomic number of each atom, the information whether the atom lies on the surface or not, the nearest neighbor relation of the atom in a unit cell and the information whether the atom is included only in the strain calculation or in both the strain and electronic calculation. In the second part, NEMO 3-D by default calculates the strain in the system based on an atomistic valence force field (VFF) approach. If desired, the strain calculation can be deactivated. This option is useful, if one wants to investigate structures without including possible strain effects, for example.

Subsequent to the calculation of the strain profile, NEMO 3-D starts computing the single-particle energies and wave functions using a 20 band atomistic nearest neighbor tight-binding model. The computation of the electronic structure is algorithmically and computationally more challenging than the strain calculation and involves handling of matrices on the order of millions. Available algorithms and solvers for the electronic structure calculation in NEMO 3-D include the PARPACK library and a custom implementation of the Lanczos method.[13] From the single-particle eigenstates, NEMO 3-D allows post processing calculations of various physical properties such as optical matrix elements or piezoelectric potentials and the graphical display of wavefunctions using Rappture.[13]

2. INTRODUCTION TO QUANTUM DOTS

The general structure of a quantum dot can be described roughly as a semiconductor, which is surrounded on a nanometer scale by a semiconducting material of larger bandgap. A quantum dot may also be characterized as a potential well with discrete energy states which result from three dimensional quantum confinement. The formation of discrete atomic-like energy states is a key characteristic of quantum dots. It is one reason why quantum dots are often referred to as artificial atoms.
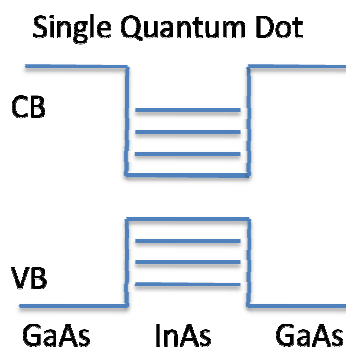
Figure 2.1 Single InAs quantum dot, quantitative band diagram

Typical dimensions of a quantum dot range from ~ 10-20nm in lateral and ~ 5nm in vertical direction. Commonly used semiconductor materials for quantum dot fabrication include GaAs, InAs or GaInAs.

Single quantum dots share characteristics resembling those of single atoms (e.g. Stark Effect). If we bring individual quantum dots close enough together on a nanometer scale, they can interact and couple quantum mechanically with each other and form structures resembling the behavior of molecules. Investigation of quantum dot structures therefore illustrates a way to study quantum mechanics on a nanometer scale rather than an atomic scale. Quantum dots can be custom designed for a wide variety of applications ranging from semiconductor devices to biological applications. Prominent examples of quantum dot applications include QD light emitting diodes, QD lasers or QD biological markers.

Quantum dots are also extensively used in studies on quantum computing and quantum communication. There are various methods existing today to fabricate quantum dots. One widely used method highlighted here is the self-assembly of quantum dots using molecular beam epitaxy - also known as the Stranski-Krastanov growth method. Depicted below (Figure 2.2) are the general steps of a growth process for a sample GaAs/InAs quantum dot structure.
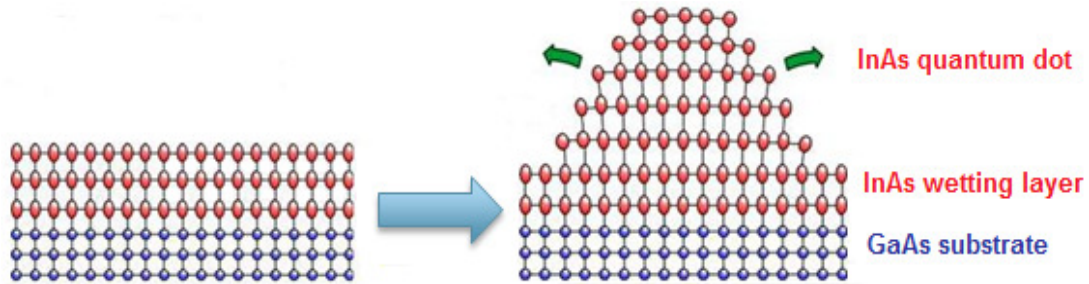
Figure 2.2 Stranski-Krastanov growth method, [9]

In our example, InAs layers (InAs wetting layer) are deposited on top of a GaAs substrate. The key element here is that the lattice constants of GaAs and InAs are not identical. This mismatch of lattice constants leads to a strained system. The strain in the system continues to increase further as more InAs layers are being deposited on the GaAs substrate. At a critical wetting layer thickness the strain is sufficiently high to enable the formation of quantum dots out of the InAs wetting layer. Quantum dots appear in different shapes and forms - such as dome-shaped, pyramidal or truncated-pyramidal.

3. QUANTUM CONFINED STARK EFFECT

3.1 QCSE in single quantum dots

In chemistry, the Stark effect describes the shifting and splitting of spectral lines of atoms and molecules in the presence of an applied external electric field. Very similar to the Stark effect is the Quantum Confined Stark Effect, which describes the effect of external electric fields on the absorption spectrum in semiconductor quantum wells and quantum dots. Tunability of the absorption spectrum based on the QCSE is an efficient way for making optical modulators and self-electro-optic effect devices. [48]

The work in this Studienarbeit focuses on the theoretical study of the QCSE in single quantum dots and vertically stacked quantum dot pairs. All the simulations were carried out using 3-D NanoElectronic Modeling (NEMO 3-D). We first present a theoretical study of the Quantum Confined Stark Effect in a GaInAs single quantum dot.
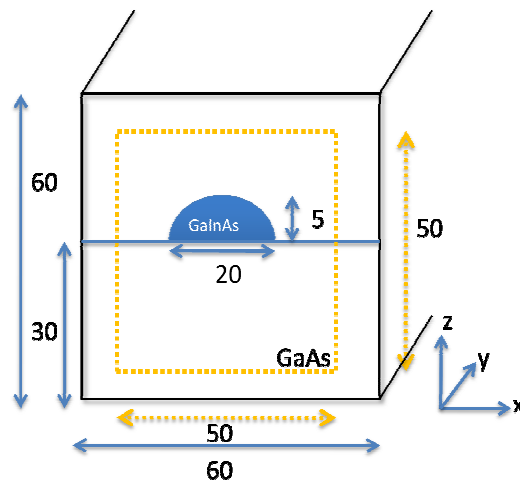
Figure 3.1 Single GaInAs quantum dot embedded in GaAs substrate, implemented in NEMO 3-D

Figure 3.1 shows the schematic of the single quantum dot, which is studied here. The dome-shaped GaInAs dot is embedded in a GaAs barrier material. The dot has a diameter of 20nm and height of 5nm and is placed on top of a 1nm thick GaInAs wetting layer.

To capture the effects of long-range strain fields penetrating into the barrier material, the strain domain is chosen sufficiently large. The strain domain comprises a box with side lengths of 60, 60 and 68nm. The electronic structure calculation is done within the box outlined by the yellow dashed lines. The electronic domain has a size of 50x50x50nm. Figure 3.2 shows a graphical representation of the first three electron states (E1,E2,E3) and the uppermost hole state H1 for no electric field applied and viewed from the top of the structure (-z direction).
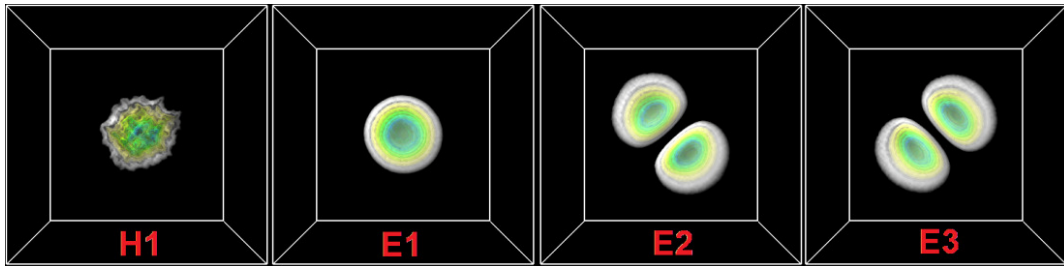
Figure 3.2 First three electron states and uppermost hole state of the single quantum dot structure described in Figure 3.1, obtained from NEMO 3-D and Rappture

To investigate the Quantum Confined Stark Effect under varying electric field strengths, we apply an electric field in positive z-direction and sweep the electric field strength from -15kV/cm to 15kV/cm. A complete simulation run for one electric field value carried out on the Coates cluster machines with 56 processors took approximately 5-6 hours. Figure 3.3 shows the energy of exciton (E1-H1) plotted against the electric field. In correspondence with published literature on single quantum dots, our results obtained from NEMO 3-D show a parabolic Stark shift. [49]
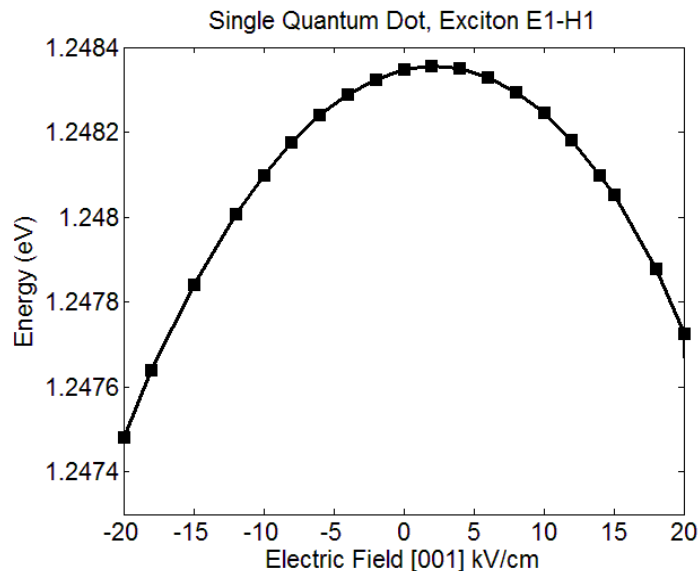
Figure 3.3 Exciton E1-H1, single quantum dot structure, see Figure 3.1.
results obtained from NEMO 3-D

For further investigation on the parabolic Stark shift behavior, figure 3.4 shows a qualitative sketch of the band diagram. Due to carrier confinement in all three spatial dimensions, discrete levels form within the quantum dot. Depicted in the figure are the lowest electron level E1 and the uppermost valence band hole state H1. If an electric field is applied along the growth direction of the quantum dot as shown in the figure, the energy difference E_g between E1 and H1 reduces.
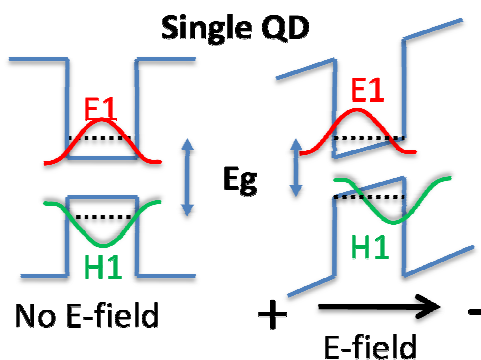
Figure 3.4 Effect of electric fields in single quantum dots

Due to the tilted potential profile in the case of an applied bias, E1 shifts towards the lower left corner of the well and thus decreases in energy. H1 on the other hand, moves up in energy towards the upper right corner of the well. The net effect is thus a lowering of the energy band gap energy (E1-H1). Figures 3.5a and b show the simulated results of the single states E1 and H1 as a function of electric field. The vertex of the parabola of H1 is not centered on zero electric field. This behavior can be attributed to strain effects and the general asymmetry of the dome-shaped quantum dot.
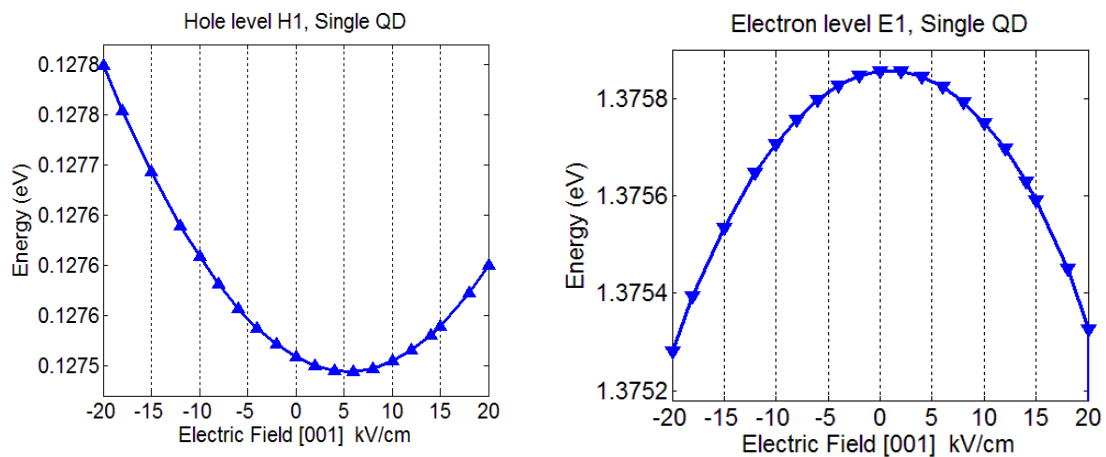
Figure 3.5 a) Hole level H1 and b) electron level E1 of single quantum dot structure (Fig. 3.1) plotted against electric field

3.2 QCSE in vertically stacked quantum dots

In the following, we present a theoretical study on the Quantum Confined Stark Effect in vertically stacked quantum dot structures. The Quantum Confined Stark Effect in vertically stacked quantum dots can exhibit parabolic as well linear dependence on the electric field. Whether we observe linear or parabolic dependence is largely determined by the location of the hole and electron state forming the exciton under investigation.
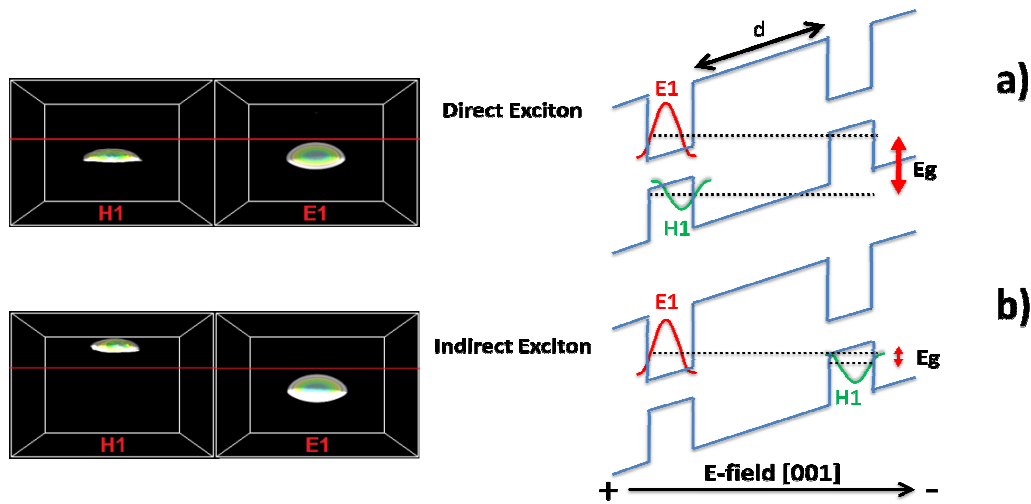
Figure 3.6 Quantitative depiction of direct and indirect exciton. If both hole and electron are in the same dot (direct), if electron and hole are in different dots (indirect)

Figure 3.6 illustrates the direct and indirect exciton in the band diagram representation. Characterized by the slope of the potential, the electric field in both the upper and lower band diagram is of equal magnitude. In figure 3.6 a) the electron and hole state are in the lower quantum dot and thus form a direct exciton. In figure 3.6 b), the hole state H1 is located in the upper dot, whereas E1 is still in the lower dot. Since the energy band gap E_g in figure 3.6 b) is smaller than E_g in figure 3.6 a), a larger Stark shift will be observed for the indirect exciton. The structure considered in our study on vertically stacked quantum dots is depicted in figure 3.7 and shows two vertically stacked dome-shaped GaInAs quantum dots. Both dots have identical diameter and height sizes of 20 and 5 nm, respectively. The dots are surrounded by a GaAs substrate of side lengths 60, 60 and 68nm and placed on top of 1nm thick GaInAs wetting layers. The dimensions of the electronic calculation domain (50x50x36nm) are marked by the yellow dashed lines. The distance between the quantum dots as measured from the wetting layers is 12 nm. Just as in the single quantum dot structure, the electric field is applied in positive z-direction and varied from -20 kV/cm to 20 kV/cm.
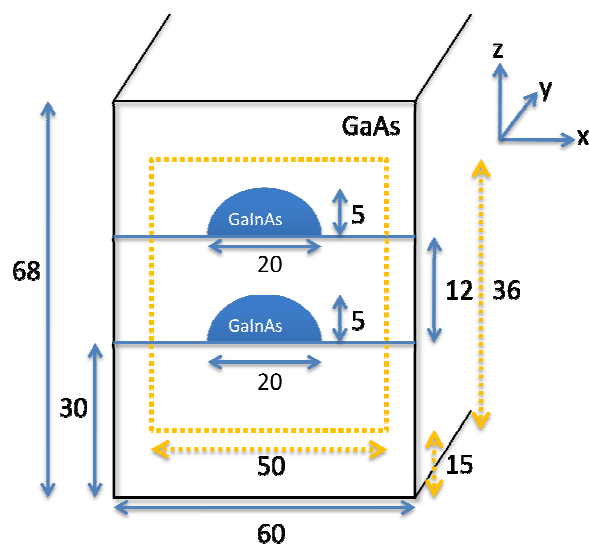
Figure 3.7 Two vertically stacked GaInAs quantum dots embedded in GaAs substrate, structure as implemented in NEMO 3-D
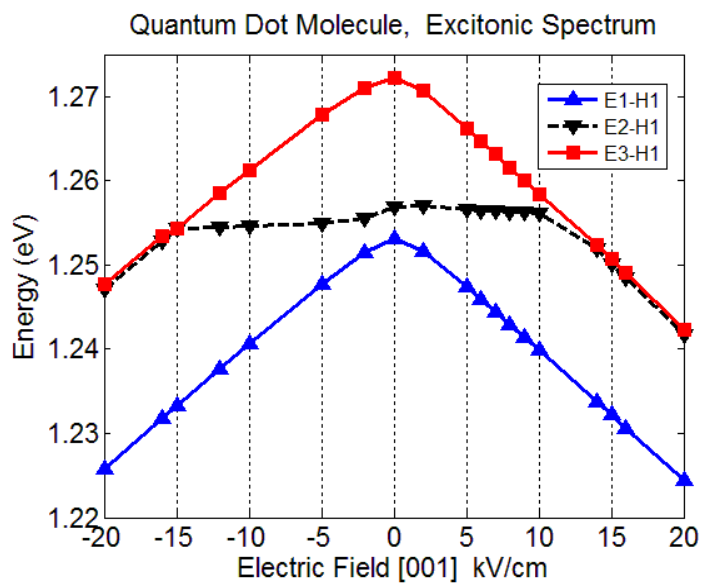
Figure 3.8 Exciton spectrum of vertically stacked quantum dot structure, excitons E1-H1 and E3-H1 are indirect, whereas E3-H1 is either indirect or direct

Figure 3.8 shows the simulated excitonic spectrum of the quantum dot molecule obtained from NEMO 3-D. Three excitons labeled E1-H1, E2-H1 and E3-H1 are displayed. Excitons E1-H1 and E3-H1 are indirect, whereas exciton E2-H1 changes from direct to indirect at different electric field strengths. To further elucidate the obtained exciton spectrum, figure 3.9 shows wave plots of the uppermost hole state and the first three electron states for various electric field strengths. For example, at an electric field strength of 5kV/cm, exciton E2-H1 is direct (E2 and H1 both in upper dot). This explains the smaller Stark shift observed for exciton E2-H1. On the other hand, as we increase the bias beyond 10 kV/cm, E2 will eventually move into the lower dot. Exciton E2-H1 then changes its type from direct to indirect, which will also be reflected in a stronger Stark shift.
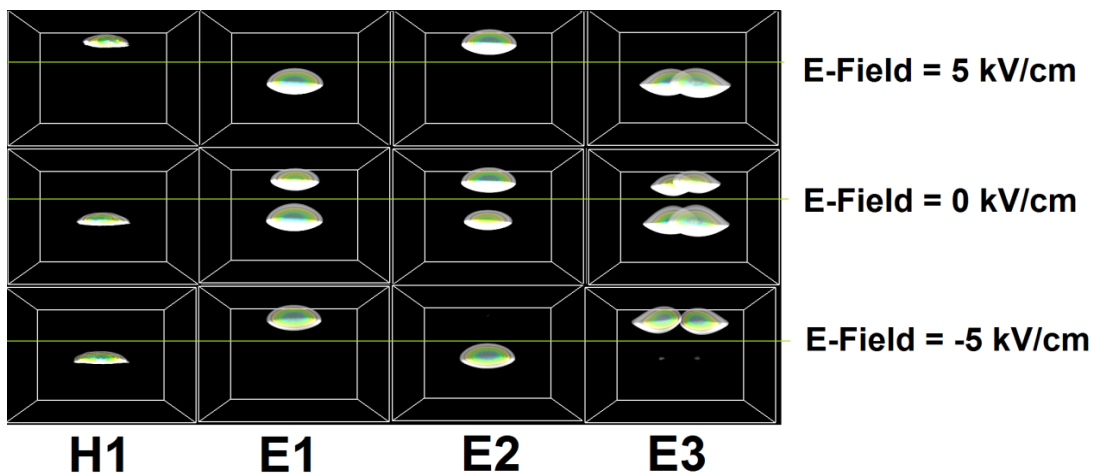
Figure 3.9 wave function plots of the first three electron states and uppermost hole state for different electric field values, vertically stacked quantum dot structure (fig.3.1)
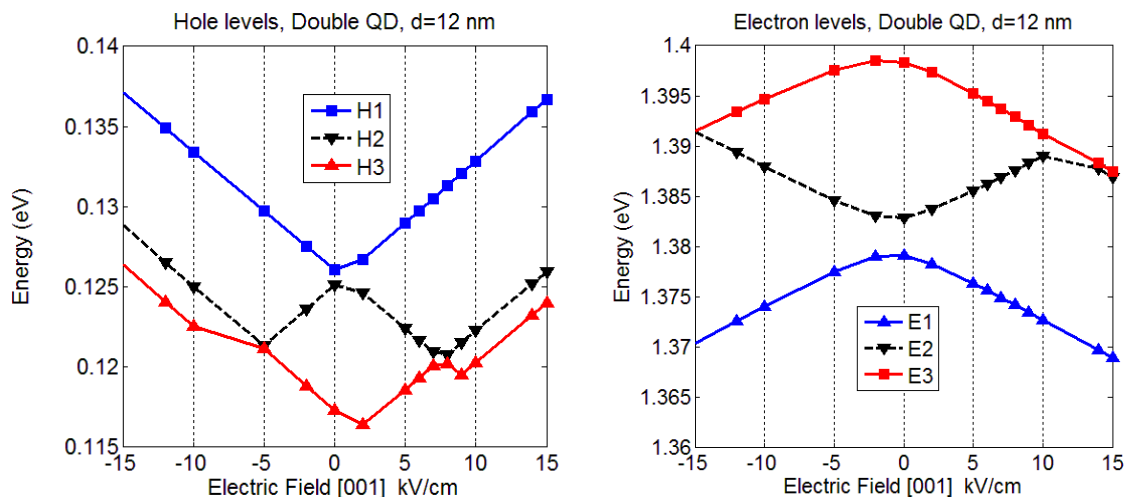
Figure 3.10 single electron and hole state energies plotted against electric field, vertically stacked quantum dot structure with d= 12 nm

In the following, we investigate theoretically the effect of varying interdot distances d on the Quantum Confined Stark Effect. In this Gedankenexperiment, we change the interdot distance in our quantum dot molecule structure from d=12nm to d= 5nm. Figure 3.11 shows the new geometry constructed in NEMO 3-D. We again consider two vertically stacked quantum dots with identical diameter and height.
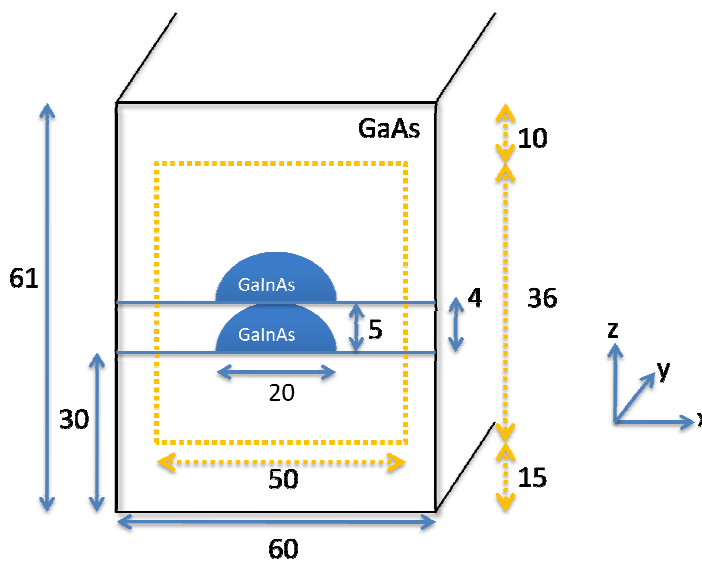
Figure 3.11 Two vertically stacked GaInAs quantum dots with interdot separation of d=5 nm, structure is simulated using NEMO 3-D
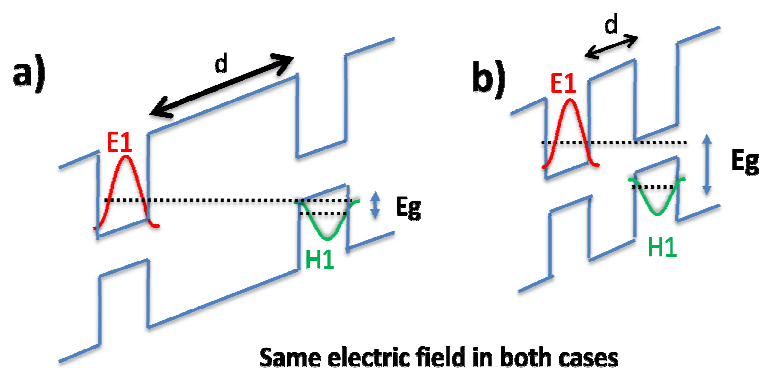
Figure 3.12 Band diagram of vertically stacked quantum dot structure for a) large dot separation and b) small dot separation

To qualitatively illustrate the effects of varying interdot separation distances, consider the band diagrams depicted in figure 3.12 a, b). In both band diagrams, the same electric field is applied. In figure 3.12 b) however, the distance d between the dots is reduced. This leads to a shorter "lever arm" and thus a smaller Stark shift for the same electric field strength. Therefore one can conclude that a smaller dot separation d results in less pronounced Stark shifts. In our simulations using NEMO 3-D, we could successfully verify these effects of varying interdot distances. Figure 3.13 shows a comparison of exciton E1-H1 for the two different interdot separations d= 5nm and d= 12nm based on the quantum dot structures in figure 3.1 and figure 3.11. In accordance with theory, we observe a drastically reduced Stark shift in the case of d= 5nm. Furthermore, we note that the maxima of the curve for d=5 nm is not centered at zero electric field. This asymmetry can be attributed to stronger strain fields in the case of smaller dot separations. As the quantum dots separation decreases, the coupling due to strain and quantum mechanical interaction effects become more pronounced.
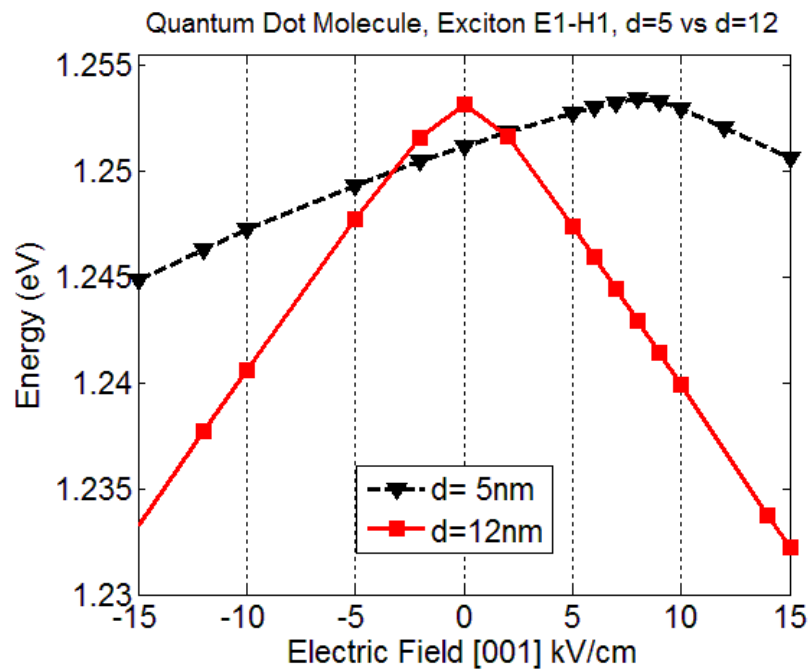
Figure 3.13 Comparison of Stark shift for different interdot separation distances, simulations are based on quantum dot structures outlined in Fig. 3.1 and Fig. 3.11

4. ATOMISTIC MODELING OF AN EXPERIMENTAL GaAs/InGaAs QUANTUM DOT MOLECULE USING NEMO 3-D

4.1. Abstract

Atomistic electronic structure calculations are performed to study the coherent inter-dot couplings of the electronic states in a single InGaAs quantum dot molecule. The experimentally observed excitonic spectrum [12] is quantitatively reproduced, and the correct energy states are identified based on a previously validated atomistic tight binding model. The extended devices are represented explicitly in space with 15 million atom structures. An excited state spectroscopy technique is presented in which the externally applied electric field is swept to probe the ladder of the electronic energy levels (electron or hole) of one quantum dot through anti-crossings with the energy levels of the other quantum dot in a two quantum dot molecule. Such a technique can be applied to estimate the spatial electron-hole spacing inside the quantum dot molecule as well as to reverse engineer the quantum dot geometry parameters such as the quantum dot separation. Crystal deformation induced piezoelectric effects have been discussed in the literature as minor perturbations lifting degeneracies of the electron excited (P and D) states, thus affecting polarization alignment of wave function lobes for III-V Heterostructures such as single InAs/GaAs quantum dots. In contrast, this work demonstrates the crucial importance of piezoelectricity to resolve the symmetries and energies of the excited states through matching the experimentally measured spectrum in an InGaAs quantum dot molecule under the influence of an electric field. Both linear and quadratic piezoelectric effects are studied for the first time for a quantum dot molecule and demonstrated to be indeed important. The net piezoelectric contribution is found to be critical in determining the correct energy spectrum, which is in contrast to recent studies reporting vanishing net piezoelectric contributions.

4.2. Introduction

4.2.1 Motivation and Background of Problem

Quantum dots grown by strain driven self-assembly attract much interest because they can be used to implement optical communication and quantum information processing [1, 2]. Recently, significant advancements in providing good stability, high repetition rate, electroluminescence, and controlled coupling have made III-V quantum dots a potential candidate for quantum computers. Based on single qubit (quantum bit) realization with an exciton in a single quantum dot [3], optical quantum gates also have been obtained with both an exciton and a biexciton within one dot [4]. Coupled quantum dot molecules (QDMs), therefore, are good candidates for spin-based [5], charge-based [6], and exciton-based [7, 8] qubits. It is desirable to excite single excitons with external electric fields. Vertically stacked QDMs have been suggested to host single or double qubits; these can then be controlled by optical pulses, electrical fields, or magnetic fields [7-11]. However, a very basic requirement necessary for realizing qubits in these structures is the prior achievement of entangled states between the two dots.

In a recent experimental study [12], coherent quantum coupling in QDMs has been observed with different separation distances between two dots forming a QDM under the applied bias. However a detailed quantitative study for the identification of the states in the spectrum and their coupling under linear and quadratic piezoelectric effects has been missing. The theoretical study accompanied with the experiment [12] is based on a single band effective mass model and considered only two lowest conduction band (E_1 and E_2) energy levels and two highest valence band (H_1 and H_2) energy levels. Thus the figure 3(b) in reference [12] plots only one anti-crossing ($E_1 \leftrightarrow H_1$) and compares it to the experimental measurement.

Moreover, it did not take into account the effects of the nonlinear piezoelectricity, because the nonlinear piezoelectric field polarization constants [24] were not available at the time of this study in 2005.

Thus the published study did not include the symmetries of individual quantum dots nor did it model the energy state couplings quantitatively. In a quantum dot molecule, each quantum dot possesses a ladder of electronic energy levels, which give rise to multiple anti-crossings due to the electrical field induced Stark shift. It is therefore essential that more than two electron and hole energy levels should be considered to identify the correct energy states in the experimental measurements.

In this work, we present an atomistic theoretical analysis of the experimental measurement including alloy randomness, interface roughness, atomistic strain and piezoelectric induced polarization anisotropy, and realistic sized boundary conditions, which we believe is essential to fully understand the complex physics of these multi-million atom nanostructures [16]. Both linear and nonlinear components of the piezoelectric field are included. The net piezoelectric field is found to be critical to resolve the symmetries and energies of the excited states. Our theoretical optical transition strengths match with the experimental quantum dot state coupling strengths.

Furthermore, we sweep the externally applied electrical field from zero to 21kV/cm to probe the symmetry of the electron states in the lower quantum dot based on the inter-dot energy level anti-crossings between the lower and the upper quantum dots. Such „level anti-crossing spectroscopic‟ (LACS) analysis [37] can be used for a direct and precise measurement of the energy levels of one quantum dot placed near another quantum dot in the direction of the applied electrical field. It can also be helpful to quantitatively analyze „tunnel coupling energies‟ of the electron and hole energy states through inter-dot energy level resonances in the single quantum dot molecule configuration predicted for „quantum information technologies‟ [12].

Finally the spacing between the anti-crossings and electrical field induced stark shifts allow us to „reverse engineer‟ the separation between the quantum dots inside the quantum dot molecule. Quantum dot molecules grown by self-assembly are mechanically coupled to each other through long-range strain originating from lattice mismatch between the quantum dot and the surrounding buffer. Despite the symmetric shape of the quantum dots (dome or lens shape), the atomistic strain is in general inhomogeneous and anisotropic, involving not only hydrostatic and biaxial components but also non-vanishing shear components [16, 26, 27].

Due to the underlying crystal symmetry theoretical modeling of these quantum dot molecules requires realistic boundary conditions to capture the correct impact of long-range strain on the electronic spectrum typically extending 30 nm into the substrate and 20 nm on both sides in the lateral direction. A detailed analysis of strain induced coupling and shifts in band edges of identical and non-identical quantum dots has been presented in earlier publications [22, 36, 38].

4.2.2. Past Studies of Piezoelectric Effects

III-V Heterostructures such as InGaAs/GaAs quantum dots show piezoelectric effects originating from diagonal and shear strain components. The asymmetric piezoelectric potentials are critical in determining the correct anisotropy of electron P-states [23-29]. Recent studies based on atomistic pseudopotentials suggest for single InAs quantum dots [24, 25] that linear and quadratic piezoelectric effects tend to cancel each other, thus leading to an insignificant net piezoelectric effect. Another study based on a k.p continuum method [30] used experimental polarization constants (see first row in table 1), which overestimated the piezoelectric effect by 35% to 50% for coupled quantum dot systems [23].

This work, for the first time, based on realistically sized boundary conditions and a three-dimensional atomistic material representation, takes into account the correct atomistic asymmetry and built-in electrostatic fields. Linear and quadratic polarization constants (see table 1) recently calculated using ab-initio calculations [23] are used to study the impact of piezoelectric effect on excitonic spectra. Our calculations on a QDM show a non-vanishing net piezoelectric effect, which is critical in reproducing experimental excitonic spectra [12]. Such non-vanishing piezoelectric potentials in single quantum dots have also been predicted recently [26].

However, previous studies in the literature so far [23-30] describe piezoelectric effects as merely small perturbations that lift excited states (P and D -states) degeneracies (increase their splitting) and/or flip the orientation of wave function lobes.

This work is the first evidence that inclusion of the piezoelectric effect is indispensable to reproduce an experimentally observed excitonic spectrum in a quantum dot molecule system, and to identify the correct energy states. Furthermore, optical transition intensities are calculated to characterize dark and bright excitons and matched with experimentally obtained transition strengths.

4.2.3. NEMO 3-D Simulator

In this letter, an experimentally observed optical spectrum [12] is reproduced and the excitonic states are identified using the NanoElectronic MOdeling tool (NEMO 3-D) [13-15]. NEMO 3-D enables the atomistic simulation and computation of strain and electronic structure in multi-million atoms nanostructures. It can handle strain and electronic structure calculations consisting of more than 64 and 52 million atoms, corresponding to nanostructures of $(110 \text{ nm})^3$ and $(101 \text{ nm})^3$, respectively [14, 15]. Strain is calculated using an atomistic Valence Force Field (VFF) method [18] with anharmonic corrections [31]. The electronic structure calculation is performed using a twenty band sp^3d^5s* nearest neighbor empirical tight binding model [17]. The tight binding parameters for InAs and GaAs have been published previously and are used without any adjustment [17]. The bulk-based atom-to-atom interactions are transferred into nano-scale devices, where no significant bond charge redistribution or bond breaking is expected and strain is typically limited to around 8%. The strain and electronic structure properties of alloys are faithfully reproduced through an explicit disordered atomistic representation rather than an averaged potential representation. The explicit alloy representation also affords the ability to model device-to-device fluctuations, which are critical in today's devices. For realistic semi-conducting nano-scale systems our tight binding approach, employed in NEMO 3-D, has been validated quantitatively against experimental data in the past through the modeling of the Stark effect of single P impurities in Si [19], distinguishing P and As impurities in ultra-scaled FinFET devices [20], the valley splitting in miscut Si quantum wells on SiGe substrate [21], and sequences of InAs quantum dots in InGaAs quantum wells [16].

4.2.4. Simulated Geometry

Figure 4.1(a) shows the simulated geometry, which consists of two vertically stacked lens shaped $In_{0.5}Ga_{0.5}As$ quantum dots separated by a 10nm GaAs buffer. As indicated in the experiment [12], the modeled upper quantum dot is larger in size (*Base=21nm*, *Height=5nm*) as compared to the lower quantum dot (*Base=19nm*, *Height=4nm*). In the lateral dimensions, the GaAs buffer size is set to 60nm with periodic boundary conditions. The modeled GaAs substrate is 30nm deep and the lattice constant is fixed at the bottom. A GaAs buffer with large lateral depth has been used to correctly capture the impact of long range strain and piezoelectric effects, which is critical in the study of such quantum dot devices [13, 14, 16, 26, 27]. The quantum dots are covered by another 30nm GaAs capping layer, where atoms are allowed to move at the top layer subject to an open boundary condition.

The electronic structure calculation is conducted over a smaller domain embedded within the strain domain using closed boundary conditions. Since the electronic states of interest are closely confined inside the quantum dots a smaller electronic domain size is sufficient to model the confined electronic states. The strain domain comprises a volume of ~15 million atoms, and the electronic domain a volume of ~9 million atoms. In accordance to the experiment, a static external electric field ($\vec{F}$) is applied in [001] growth direction and varied from zero to 23kV/cm.
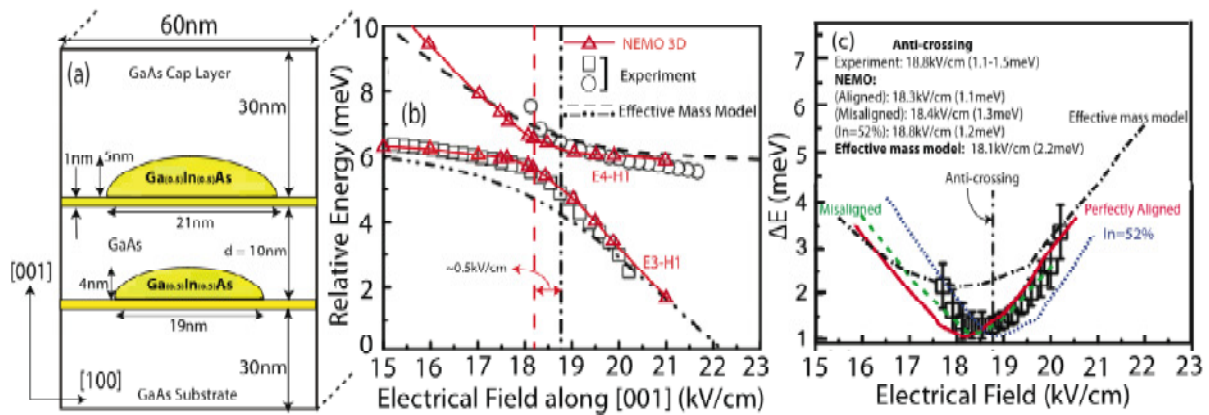
Figure 4.1: (a) Model system consisting of two lens shaped $In_{0.5}Ga_{0.5}As$ quantum dots vertically stacked and separated by a 10nm GaAs buffer as described in the experiment. Both quantum dots are placed on 1nm thick $In_{0.5}Ga_{0.5}As$ wetting layers. Substrate and cap layer thicknesses are 30nm. (b) NEMO 3D excitonic spectra (red triangles) for perfectly aligned quantum dots are compared with experimental measurement (black circles and squares) [12] and effective mass calculation [12] (dotted lines) [12]. The NEMO 3-D calculations match experiment quantitatively and give a much better estimate of tunnel coupling energy than the effective mass model [12]. (c) Difference energy of excitons (*E3,H1*) and (*E4,H1*) in (b) is compared for various cases. Black squares with error bars are from experimental data. Solid line (red) is from NEMO 3-D structure in (a). Broken line (green) is for NEMO 3-D where the upper quantum dot in (a) is shifted to the right by 0.5nm. Dotted line (blue) is from NEMO 3-D with $In_{0.52}Ga_{0.48}As$ quantum dots. Broken line with dots (black) is from the effective mass calculations [12]. A quantitative match of NEMO 3-D with experiment is evident. Small variations in quantum dot location and alloy composition insignificantly change the electrical field of the anti-crossing and barely influence the exciton energy difference.

4.3. Results

4.3.1. Experimental Emission from Excited States

Figure 4.1(b) plots the excitonic energies as a function of applied bias. The curves indicated by circle and square data points are from experimentally obtained Photoluminescence measurements [12]. The measurements identify two bright excitonic emissions forming a tunable, coherently coupled quantum system. The triangle data points are from NEMO 3-D simulations. The excitonic spectra calculated here are based on a simple energy difference of the single electron and hole eigenenergies. The charge to charge interaction will reduce the optical gap by around 5meV which we are ignoring in our calculations. Based on the simulation results, two excitons (E_3,H_1) and (E_4,H_1) are identified to match the experiment.

Figure 4.1(c) compares the calculation of the exciton splitting $\Delta E = (E_4,H_1)-(E_3,H_1)$ obtained from NEMO 3-D with the experiment and a single band effective mass calculation [12]. The splitting at the anti-crossing point (ΔE_{min}), referred to as the "tunneling coupling energy" [12] or the "anti-crossing energy" [37] is found to be ~1.1meV, which closely matches the experimental value of 1.1-1.5meV. On the other hand, the effective mass model significantly overestimates the tunneling coupling energy, predicting a value of ~2.2meV. Quantum dot molecules grown by self-assembly processes are neither perfectly aligned vertically [34], nor can the „In" fraction of the quantum dot material be precisely determined [35]. These parameters are subject to slight variations during self-organization of the quantum dot nanostructures.

Theoretical studies using NEMO 3-D on horizontally misaligned quantum dots (lateral misalignment = 0.5nm) and slight variation in the „In" fraction ($In_{0.52}Ga_{0.48}As$ quantum dots instead of $In_{0.5}Ga_{0.5}As$ quantum dots) show that these difficult to control experimental imperfections can shift anti-crossing points to slightly higher electrical field values. For example, the anti-crossing point is found to be at 18.5kV/cm for the misaligned quantum dots and at 18.7kV/cm for increased indium fraction concentration as compared to 18.3kV/cm for perfectly aligned $In_{0.5}Ga_{0.5}As$ quantum dots.

The exciton tunnel coupling energies appear to be almost insensitive to such experimental variations. The theoretical values show a close quantitative match with the experimental value of 18.8kV/cm, regardless of the small variations in quantum dot alignment and small alloy composition variations.

4.3.2. Observations of Anti-Crossings within the Experimental Field Range

Figure 4.2(a) shows the spatial distribution of the single particle energy states in a schematic band edge diagram with piezoelectric field effects at zero electrical field. The wave function plots are inserted corresponding to each energy state to indicate their spatial occupation inside the quantum dot molecule and their single atom or molecular character. If the energy and position of H_1 is kept fixed and used as the center of the electrical field lever arm shift, the application of an external [001] electrical field will tilt the band edges such that the lower quantum dot energy levels will move down in energy. Since the center of the electrical field lever arm shift is set at the position of the upper quantum dot, the lower quantum dot energy levels will exhibit a strong shift in energy whereas the upper quantum dot energy levels will experience only a small Stark shift. As the lower quantum dot energy levels are shifted down by the electrical field, they anti-cross with the energy levels of the upper quantum dot and hence give rise to resonances.

Figure 4.2(b) shows the new distribution of the energy levels at the electrical field strength of 15kV/cm. At 15kV/cm it is quite evident that the lowest two electron states (E_1 and E_2) have already moved into the lower quantum dot. The excited electron state E_3 located in the upper quantum dots creates a direct exciton (E_3, H_1) with H_1. The excited state E_4, is in the lower quantum dot and forms an indirect exciton (E_4, H_1) at = 15kV/cm. It can be anticipated that with further increase in the electrical field >15kV/cm, the conduction band edge will be tilted further. This will result in a decrease in the energy of E_4. The energy state E_3 will, therefore, anti-cross with the energy state E_4. This turns „off" the optically active exciton (E_3, H_1) and turns „on" the optically inactive exciton (E_4, H_1) as observed in the experiment [12].

Our calculations shown in figure 4.1(b) demonstrate the anti-crossing between the excitons (E_3,H_1) and (E_4,H_1) in the range of applied bias (15kV/cm to 23kV/cm). A comprehensive spectroscopy of the energy levels for electrical fields spanning from zero to 21kV/cm is presented in figure 4.3.
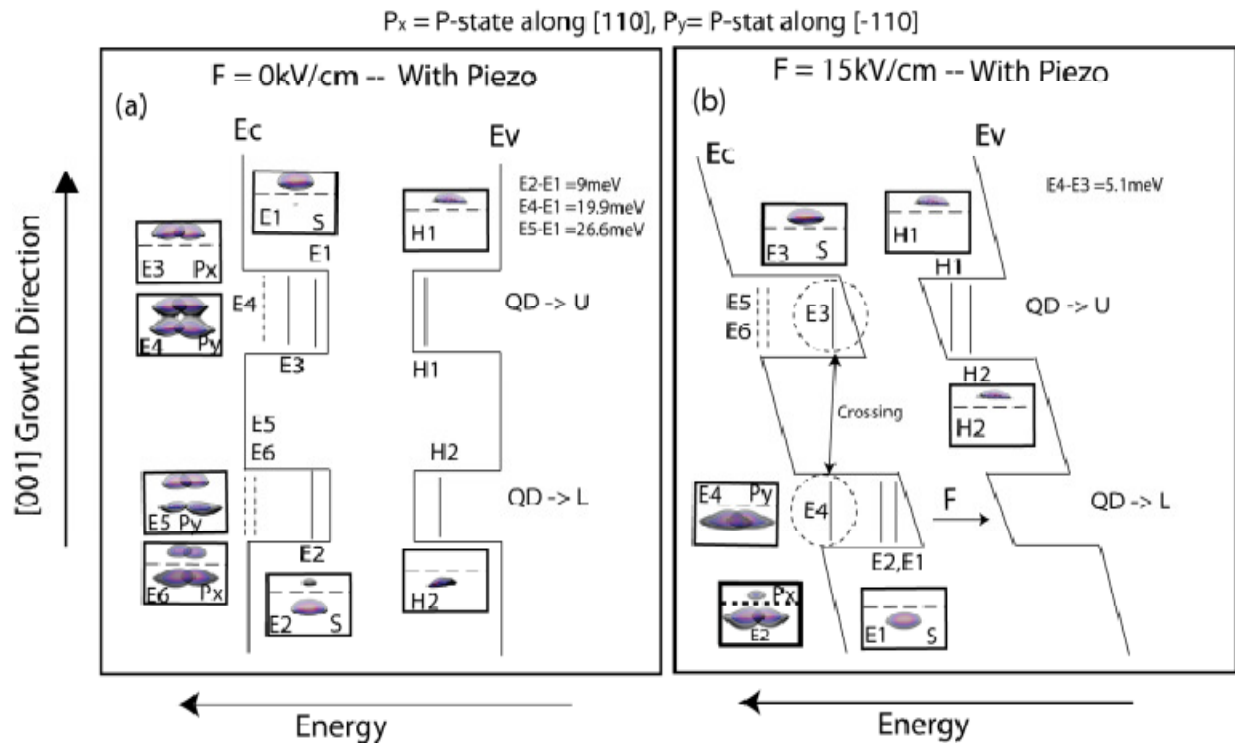
Figure 4.2: (a) Schematic lowest conduction (E_c) and highest valence band (E_v) edges with piezoelectric potential but zero external electrical field. Wave function plots are inserted for each energy state as small insets. The dotted lines in the insets separate the upper and lower quantum dots. Ground hole and electron states reside in the upper quantum dot because of its larger size [22, 36, 38]. (b) Schematic lowest conduction (E_c) and highest valence band (E_v) edges with piezoelectric potential and with 15kV/cm applied electrical field. Wave function plots are inserted for each energy state as small insets. The dotted lines in the insets separate the upper and lower quantum dots. Arrows are marked to show the tilting of band edges and the directions of movement of energy states when the electrical field is applied. The electrical field pushes E_1 and E_2 to the lower quantum dot, causing excitons (E_1,H_1) and (E_2,H_1) to be optically inactive. At 15kV/cm, E_3 makes a direct exciton with H_1 and hence will be optically active. Further increase in electrical field strength beyond 15kV/cm will push E_3 to the lower quantum dot and E_4 to the upper quantum dot resulting in an anti-crossing between E_3 with E_4 as observed in the experimental measurement [12].

4.3.3. Electronic Spectrum Spectroscopy

Figures 4.3(a, b) plot the electrical field dependence of the lowest four conduction band energy levels (electron energy states E_1, E_2, E_3, and E_4) and the highest four valence band energy levels (hole energy states H_1, H_2, H_3, and H_4) for the experimental quantum dot molecule geometry under study with (a) and without (b) piezoelectric fields. The [001] electrical field magnitude is varied from zero to 21kV/cm. The top most valence band (hole ground) state H_1 resides in the upper quantum dot at zero applied electrical field due to the larger size of the upper quantum dot and the dominance of the heavy hole (HH) band under these strain conditions [22, 36, 38]. The reference for the electrical field shift „lever arm‟ is set to the top most valence band energy level H_1 to keep it fixed at its zero electrical field value. All other energy levels are referenced to H_1.

As shown in figure 4.3(a), at the electrical field strength of $\vec{F}=0$, the ground electron state E_1 is in the upper quantum dot due to its larger size [22, 36]. E_2 is in the lower quantum dot, whereas E_3 and E_4 are in the upper quantum dot and show P_x, P_y like symmetry. The same position and character of the electronic states at $\vec{F}=0$ is also shown in figure 4.2(a) using a schematic band edge diagram. The wave function plots are inserted corresponding to each energy state to indicate their spatial occupation inside the quantum dot molecule and their single atom or molecular character. As described earlier, the application of the external electrical field tilts the conduction bands, pushing the lower quantum dot states to lower energies (see also figure 4.2(b)). On their way down to lower energies, the lower quantum dot electron energy states anti-cross with the upper quantum dot electron energy states and exhibit molecular like character. An anti-crossing results from the resonance of one quantum dot's energy state (electron or hole) with the other quantum dot's energy state when an external electrical field is applied. At the resonance point, the electron states become spatially delocalized over the two quantum dots and form bonding and anti-bonding like molecular states. The hole states remain primarily localized in separate dots.

The separation between the anti-crossings provides a direct measurement of the energy levels of the lower quantum dot, and hence enables „reverse engineering" to determine the quantum dot dimensions and symmetry. Such spectroscopic probing of the hole energy states in a quantum dot molecule has been done recently [37] and is referred to as „level anti-crossing spectroscopy". Figure 4.3(a) shows the distribution of three anti-crossings ($E_1 \leftrightarrow E_2$, $E_2 \leftrightarrow E_3$, and $E_3 \leftrightarrow E_4$) between the electron energy levels. At $\vec{F}=0$, E_1 is in the upper quantum dot and E_2 in the lower quantum dot. The first anti-crossing $E_1 \leftrightarrow E_2$ results from the resonance of the two s-type electronic states E_1 and E_2 when the electrical field is in the range of ~5kV/cm. The anti-crossing energy for $E_1 \leftrightarrow E_2$ is ~5.9meV. For electrical fields between 6kV/cm and 15kV/cm, E_1 resides in the lower quantum dot and E_2 resides in the upper quantum dot. Increasing the electrical field up to ~15kV/cm results in a second anti-crossing $E_2 \leftrightarrow E_3$ between the s-type upper quantum dot state (E_2) and the p-type lower quantum dot state (E_3). The anti-crossing energy for this s-p anti-crossing (~0.7meV) is much smaller than the previous s-s anti-crossing energy. This anti-crossing involves states that are higher in energy as measured from the relative bottom of the quantum well. The barrier height that separates/couples the states is noticeably smaller. As such, the reduced coupling strength is at first unintuitive.

The magnitude of the anti-crossing energy depends on the wave function overlap and the symmetries of the states involved [37]. The s-p anti-crossing energy will be smaller than the s-s anti-crossing energy because of the different spatial symmetries of the s- and p-states and smaller overlap between these two orbitals. Beyond $\vec{F}=15$kV/cm, both E_1 and E_2 are atomic like states confined in the lower quantum dot. Further electric field induced shifts will bring E_4 (lower quantum dot state) into resonance with E_3 (upper quantum dot state) and induce a third anti-crossing $E_3 \leftrightarrow E_4$ between the s-type upper quantum dot state and the p-type lower quantum dot state. The anti-crossing energy for $E_3 \leftrightarrow E_4$ is ~1.1meV. Since the experiment [12] was performed for electrical fields varying from 15kV/cm to 21kV/cm, the only experimentally observed anti-crossing (see figure 4.1(b)) is $E_3 \leftrightarrow E_4$.

(With Piezoelectricity)

(Without Piezoelectricity)
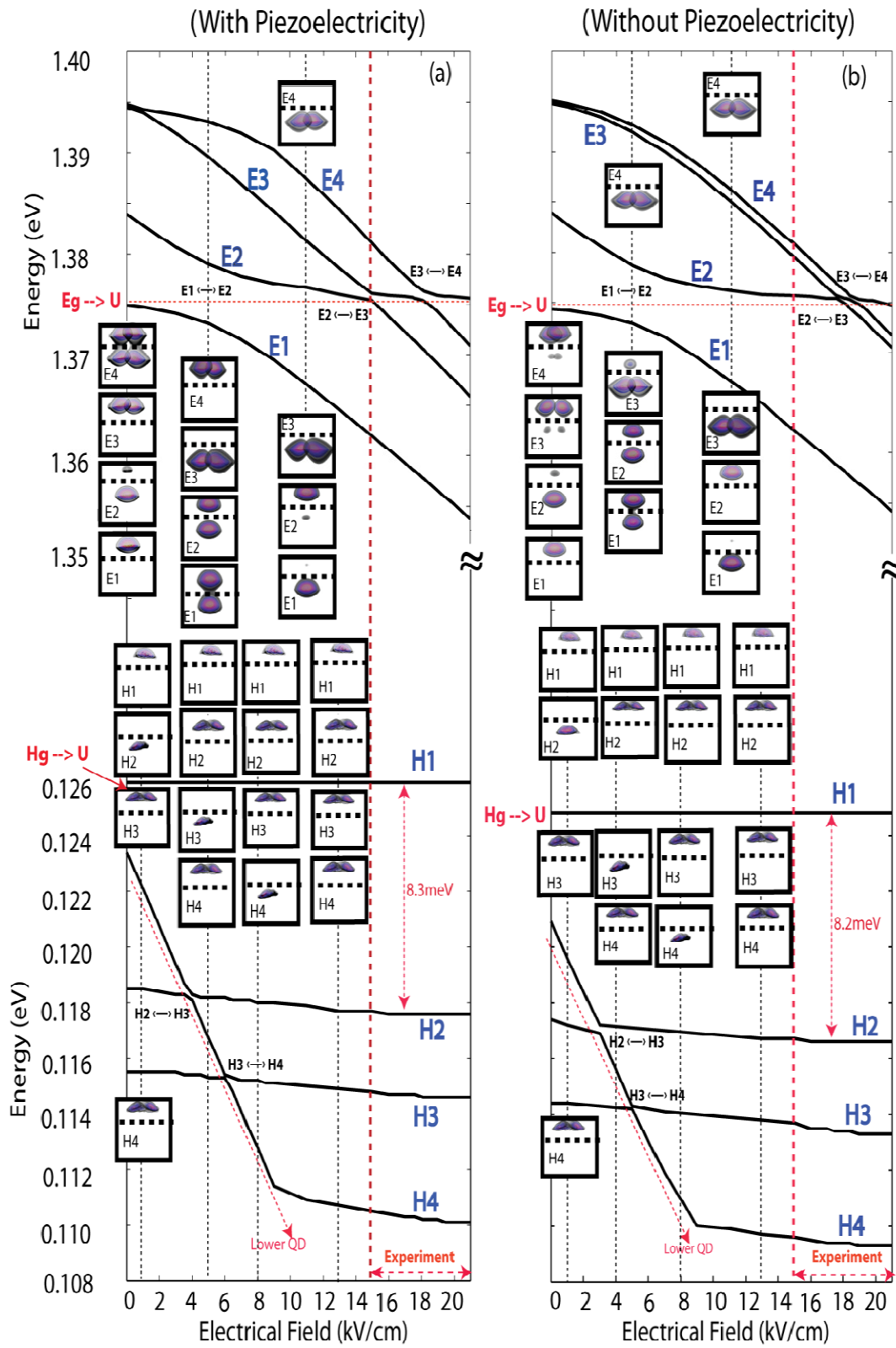
Figure 4.3: (a, b) Plot of first four electron and hole energy levels as a function of applied [001] electrical field. The electrical field is varied from zero to 21kV/cm. The H_1 energy is taken as the center of the electrical field lever arm so that its energy remains fixed at its zero electrical field value. Wave functions are inserted as small insets at critical values of electrical field to highlight the spatial position of the energy states inside the quantum dot molecule. The dotted lines in the wave function insets are marked to guide the eyes and separate the upper and lower quantum dots. Both electron and hole energy levels of the lower quantum dot exhibit anti-crossings with the energy levels of the upper quantum dot. The sequence of anti-crossings reveals the electron and hole level structure of the lower quantum dot and provides a direct measurement of the energy states in the lower quantum dot. The regions of the experimental electrical fields (from 15kV/cm to 21kV/cm) are enlarged in figure 4.3 c and d.

The strength of the electrical field induced shift in the lower quantum dot energies depends on the separation between the quantum dots, as the center of the electrical field lever arm shift is fixed at H1 in the upper quantum dot. The slope of this shift, calculated from figure 4.3(a), is $\Delta E/\Delta F \sim$ -1.33 meV kV^{-1} cm. This predicts the spatial separation between H_1 and the lower quantum dot electron states to be around 13.3nm. Since the wetting layer separation is 10nm, the center-to-center distance between the quantum dots is 11.5nm. The small difference of 13.3-11.5=1.8nm between the predicted value and the center-to-center distance of the quantum dots is due to the spatial separation between the electron and hole states in the quantum dot. The hole states tend to reside closer to the top of the quantum dot and the electron states closer to the bottom of the quantum dot [33]. This is also consistent with the slope of upper quantum dot electron energy shift, which is around $\Delta E/\Delta F \sim$ -0.167 meV kV^{-1} cm. This corresponds to an intra-dot electron-hole spatial separation of 1.67nm, close to the value of 1.8nm mentioned above.

The spectrum shown in figure 4.3(a) clearly shows the spectroscopic probing of the lower quantum dot electron states by the upper quantum dot state E_1. This technique is very useful to determine the geometry parameters of the molecular quantum dot. For example, if we do not know the separation between the quantum dots, the $E_1 \leftrightarrow E_2$ anti-crossing values of $\mathbf{F}$ and the slope of the energy shifts can be used to estimate the separation between the quantum dots. Regarding the quantum dot molecule in this study, E_4-E_1 is ~19.9meV as shown in figure 4.2(a) at $\vec{\mathbf{F}}$ =0. The anti-crossing between these two states occurs at ~18.3kV/cm. This gives approximately a separation of 10.87nm between the two quantum dots, which is very close to the value of ~10nm provided by the TEM measurements [12]. Thus, the spacing between the anti-crossings and the electrical field induced stark shift allow us to „reverse engineer" the separation between the quantum dots.
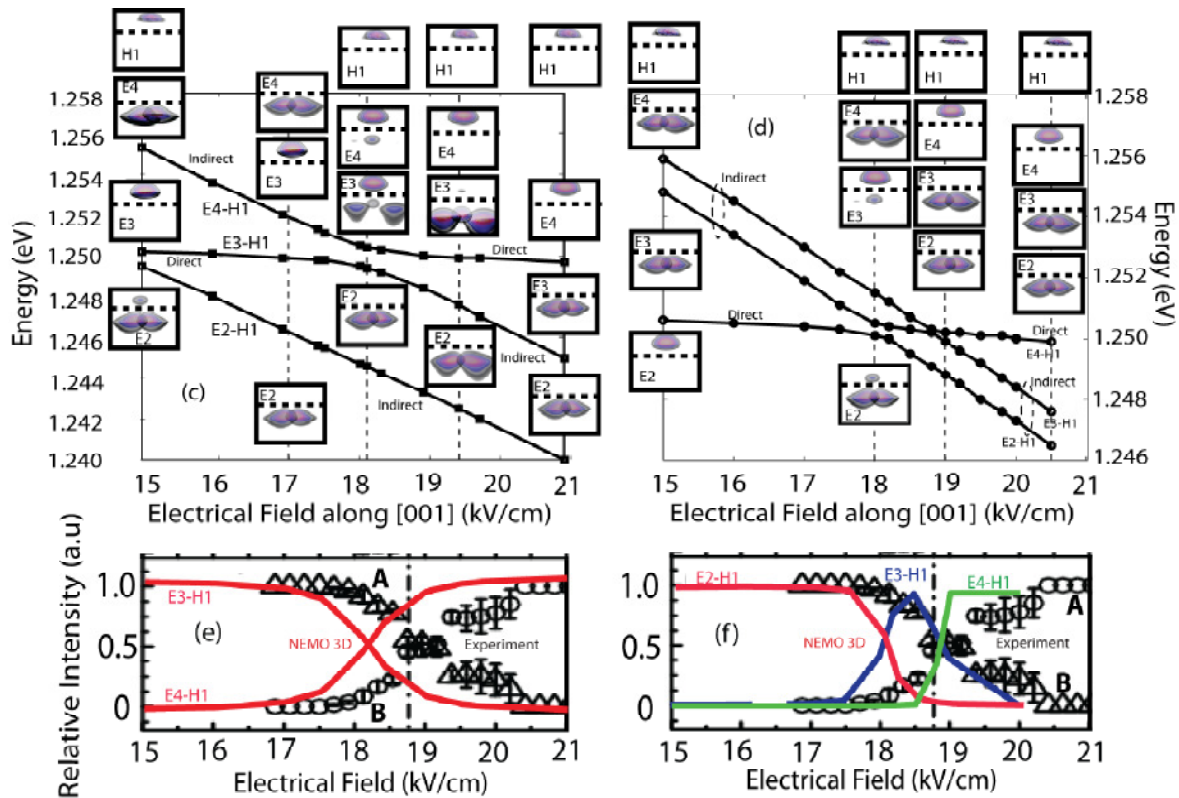
Figure 4.3 (c, d) Excitons (E_2,H_1), (E_3,H_1), and (E_4,H_1) are shown as a function of [001] electrical field without (f) and with (e) piezoelectric effects. Insets show the wave function plots at (f) 15kV/cm, 18kV/cm and 19kV/cm, (e) 15kV/cm, 18.2kV/cm, and 19.5kV/cm. The dotted lines in the wave function insets are marked to guide the eyes and separate the upper and lower quantum dots. In the case of no piezoelectricity, two anti-crossings clearly mismatch the experimental measurement [12]. (e, f) plots the relative intensity of the interband optical absorption strengths as a function of the electrical field without (d) and with (c) the piezoelectricity. The solid lines are from NEMO 3-D calculations. Circles and triangles are from experimental measurements [12]. It is clearly evident from the comparison of (c) and (d) that piezoelectricity is critical to reproduce the experimentally measured optical spectra [12].

The ground hole state H_1 resides in the upper quantum dot as shown in figure 4.2, regardless of the field strength. We therefore mark this state as the ground hole state of the upper quantum dot: $H_g \rightarrow U$. The electron ground state of the upper quantum dot is marked as $E_g \rightarrow U$ and shown as a horizontal dotted line in figure 4.3(a). The optically active exciton will always be comprised of these two ground states of the upper quantum dot. It should be pointed out that, although $E_g \rightarrow U$ is referred to as the upper quantum dot ground state, this energy state undergoes several anti-crossings with the lower quantum dot states and exhibits both atomic and molecular character at increasing electrical field strengths. More importantly, at the anti-crossing point $E_3 \leftrightarrow E_4$, the $E_g \rightarrow U$ state hybridizes with the lower quantum dot P-state. This is very critical, because it underlines the importance of piezoelectric fields. As will be shown later, piezoelectricity has stronger effects on electron P-states as compared to electron s-states.

Figure 4.3(a) also depicts the distribution of the hole energy level anti-crossings as a function of the applied electrical field. The electric field pushes the hole energy levels of the lower quantum dot further to lower energy values. Thus, by sweeping through the electric field, we can obtain a spectroscopic image of the upper quantum dot's hole energy levels when these anti-cross with the hole energy levels of the lower quantum dot. H_1 is in the upper quantum dot at zero electric field and remains so for the applied electric field direction. H_2 is in the lower quantum dot and as it moves down in energy, it couples with hole states in the upper quantum dot. This gives rise to the anti-crossings $H_2 \leftrightarrow H_3$ and $H_3 \leftrightarrow H_4$. The hole anti-crossing energies are ~0.2meV and ~0.1meV for $H_2 \leftrightarrow H_3$ and $H_3 \leftrightarrow H_4$ respectively. These hole anti-crossing energies are significantly smaller than the corresponding electron anti-crossing energies, indicating a much stronger hole localization. Notably, in the range of the experimental electric field from 15kV/cm to 21kV/cm, all of the four hole levels are in the upper quantum dot and no anti-crossings are observed. This implies that the electron states in the lower quantum dot exhibit weak optical transition strengths with the first four hole energy levels and hence are not measured experimentally.

5. IMPACT OF PIEZOELECTRICITY

5.1. Energy Spectrum Without and With Piezoelectricity

The comparison of figures 4.3(a) and 4.3(b) highlights the impact of piezoelectric fields on the energy spectrum of the quantum dot molecule under study. Piezoelectricity does not impact the hole energy spectrum significantly. The hole energy levels exhibit only a small energy shift and only minor changes are observed in the hole anti-crossings. The electron ground state energies of the two quantum dots E_1 and E_2 and the anti-crossing $E_1 \leftrightarrow E_2$ are also only shifted by a small amount. However, the excited electron states E_3 and E_4 are affected significantly.

Piezoelectricity increases the splitting between E_3 and E_4 and thus changes the position of the anti-crossing $E_2 \leftrightarrow E_3$ on the electrical field axis. With piezoelectricity considered, $E_2 \leftrightarrow E_3$ occurs outside the range of the experimentally applied electrical field. On the other hand, if piezoelectricity is included, the anti-crossing $E_2 \leftrightarrow E_3$ occurs within the range of the experimentally applied electrical field. It implies that, without piezoelectric fields included, there will be two anti-crossings in the range of the electric field from 15kV/cm to 21kV/cm. This contradicts the experimental measurements shown in figure 4.1(b). To further explain the anti-crossings in the experimental range of applied electric field, the two excitonic spectra for both cases are enlarged in figure 4.3 c) and d).

Figures 4.3 (c, d) show the three exciton energies (E_2, H_1), (E_3, H_1), and (E_4, H_1) of the system with (c) and without (d) piezoelectric potential considered as a function of applied electric field. The wave functions of H_1 as well as E_2, E_3, E_4 are depicted as insets for a number of electric field strengths. If both the electron and hole states are in the same quantum dot, the resulting exciton is called a "direct exciton". It corresponds to an optically active state with a large electron hole overlap. On the other hand, if the electron and hole states are in different quantum dots, the resulting exciton is called an "indirect exciton". It corresponds to an optically inactive state with a negligible electron and hole overlap.

Energy perturbations due to the Quantum Confined Stark Effect (QCSE) in direct and indirect excitons under applied bias exhibit different slopes: $\Delta E_{exciton} = p.\vec{\mathbf{F}}$, where p is the dipole moment of the exciton, and $\vec{\mathbf{F}}$ is the applied electric field. The exciton dipole moment is defined as: p = q.d, where „q" is the electronic charge and „d" is the spatial electron-hole separation. In the case of a direct exciton, both electron and hole are in the same quantum dot and separated by a short distance (typically d ≤ 1nm). The resulting magnitude of the Stark shift is therefore very small. In the case of an indirect exciton however, the electron and hole are in different quantum dots and separated by a large spatial distance (d ≥ 10nm in our case). Therefore, the dipole moment and the magnitude of the Stark shift will be large. [33] Figure 4.3 (c) and (d) depict the direct and indirect nature of the observed excitons over the range of applied bias. As the figures indicate, a strong (larger slope) and a weak (smaller slope) Stark effect correspond to an indirect and direct exciton, respectively.

The experimentally measured optical spectra (circles and triangles in figures 4.3(e) and 3(f)) show the relative strength of the two excitonic emissions 'A' and 'B'. At $\vec{\mathbf{F}}$ =15kV/cm, the excitonic emission 'A' is bright and 'B' is dark. As the electric field is increased, the intensity of 'A' decreases and the intensity of 'B' increases. The optical strengths of both excitons 'A' and 'B' become comparable at the electric field value of 18.8kV/cm, where these two excitons anti-cross. At higher electric field strengths, the intensity of 'A' decreases rapidly and 'B' becomes optically bright.

We compute the transition rate intensities using Fermi's golden rule as the squared absolute value of the momentum matrix: $|< E_{2or3or4}|[\vec{n},\mathbf{H}]|H_1 >|^2$, where **H** is the single particle tight binding Hamiltonian, $E_{2or3or4}$ are electron states, H_1 is the top most valence band hole state, and $\vec{n}$ is the polarization direction of the incident light [32, 39-41]. Figure 4.3(e) compares the relative transition rate intensities $I_{(E_4,H_1)or(E_3,H_1)}/(I_{(E_4,H_1)} + I_{(E_3,H_1)})$, where $I_{(E_4,H_1)}$ and $I_{(E_3,H_1)}$ are the transition rate intensities of (E_4,H_1) and (E_3,H_1) , respectively.

Figure 4.3(f) compares the relative transition rate intensities $I_{(E_2,H_1)} or I_{(E_3,H_1)} or I_{(E_4,H_1)} / (I_{(E_4,H_1)} + I_{(E_3,H_1)} + I_{(E_2,H_1)})$, where $I_{(E_2,H_1)}$, $I_{(E_3,H_1)}$ and $I_{(E_4,H_1)}$ are the transition rate intensities of (E_2,H_1) , (E_3,H_1) and (E_4,H_1), respectively. Figure 4.3(e) compares the calculated optical strengths, including piezoelectric effects, obtained from NEMO 3D with the experimental measurements. In this case, as the electric field is increased, the intensity of (E_3,H_1) reduces rapidly, whereas the intensity of (E_4,H_1) increases.

Figure 4.3(c) plots the excitonic energies (E_2,H_1), (E_3,H_1) and (E_4,H_1) as a function of the applied electrical field. E_2, which is localized in the lower dot, forms an indirect exciton with H_1 in the range of applied electric field from 15kV/cm to 21kV/cm. The optical strength of (E_2,H_1) is therefore weak and not experimentally measured. On the contrary, (E_3,H_1) is a direct exciton at 15kV/cm and experimentally measured as a strong optical peak. Increasing the electric field from 15KV/cm results in the tunneling of E_3 from the upper quantum dot to the lower quantum dot. (E_3,H_1) eventually changes its character from an optically active state to an optically inactive state at F~18.8kV/cm. In the vicinity of the anti-crossing point (F from ~17.9kV/cm to ~20.5kV/cm), the two excitons (E_3,H_1) and (E_4,H_1) are tuned into resonance and exhibit a close to equal magnitude of intensity. In that field range, the electron states (E_3 and E_4) are found to be delocalized across the two quantum dots. Note that the relative intensities of the excitons in figure 4.3(e) calculated by our model closely follow the slopes of the experimental curves. NEMO 3-D is hence able to correctly capture the dynamics of controlled coupling under resonance of excitons. The controlled coupling of quantum dots under external bias (gate voltage) is critical in the implementation of exciton qubits and may foster efforts in quantum information processing based on quantum dots.

Figure 4.3(f) compares the experimentally measured transition strengths ('A' and 'B') with our calculated transition strengths (solid lines) obtained from NEMO 3-D. Note that in this case, we explicitly did not include piezoelectric effects. The calculated transition strengths indicate three bright peaks and two anti-crossings. At F =15kV/cm, exciton (E_2,H_1) is bright and excitons $(E_3,H1)$ and (E_4,H_1) are dark. As the electric field increases, first (E_2,H_1) anti-crosses with exciton (E_3,H_1). Further increase in the electric field results in a subsequent anti-crossing between excitons (E_3,H_1) and (E_4,H_1). Figure 4.3(d) plots the corresponding excitonic energies as a function of applied electrical field. The direct and indirect nature of the excitons follows the optical transition strength patterns of figure 4.3(d). At =15kV/cm, exciton (E_2,H_1) is direct and excitons (E_3,H_1) and (E_4,H_1) are indirect. The first anti-crossing makes exciton (E_2,H_1) indirect and exciton (E_3,H_1) direct. The second anti-crossing makes exciton (E_3,H_1) indirect and exciton (E_4,H_1) direct. In short, the omission of piezoelectricity, as shown in the figures 4.3(d) and 4.3(f), results in three bright excitonic emissions, which disagrees with the experimentally measured spectra.

The anti-crossings of the electron states in the experimental electric field range involve electron P-states of the lower quantum dot. Since piezoelectric effects are more pronounced in excited states [23-26, 28, 29, 38], the correct identification of optically active states in the experimental measurements is of crucial importance. If the experimental emissions came from the ground state, piezoelectric effects would be of minor. Figures 4.3(c) and 4.3(d) clearly show that including piezoelectric effects is important to obtain the correct resonance at the point of anti-crossing. Furthermore, the field dependence of the optical intensity is also strongly dependent on piezoelectricity. We obtain the smoothly varying intensity variation as obtained in the experiment only when piezoelectric fields are included [12].

5.2. Piezoelectric Model

Piezoelectricity is calculated from electrical polarization originating from stressed crystals lacking inversion symmetry [29]. InGaAs/GaAs quantum dots are nanostructures with a lattice mismatch (~7%), which leads to long-range strain fields penetrating deep into the surrounding buffer [22, 27, 38]. The diagonal and off-diagonal (shear) strain components can result into a built-in piezoelectric polarization, which cannot be ignored. Bester et *al*. [24] and Ahmed et *al*. [27] outlined the importance of linear piezoelectric effects for single InAs quantum dots. Later, Bester et *al*. [25] highlighted the significance of the second order (quadratic) component of piezoelectricity. They concluded that the second order piezoelectric effect cancels the first order (linear) component, thus leading to a net piezoelectric effect significantly suppressed. Following their argument that the net piezoelectric effect and its impact on the excitonic spectrum is negligible, they further claimed that it is advisable not to consider piezoelectric effects at all rather than including only the linear component of the piezoelectric effect.

On the other hand, Schliwa et *al*. [28, 29] have indicated the importance of net piezoelectricity for a number of shapes and sizes of single quantum dots. The work presented here on quantum dot molecules clearly emphasizes that net piezoelectric effects cannot be neglected and are of critical importance in determining correct excitonic emission spectra in coupled dot systems that involve occupation of excited states.

In our model, the piezoelectric potential is included into the single particle Hamiltonian according to the recipe presented in references [24, 29]. First, both linear $\mathbf{P_1}$ (first order) and quadratic $\mathbf{P_2}$ (second order) polarizations are separately calculated from the strain tensor components (equations (1) and (2)) using already published polarization constants (e_{14}, β_{114}, β_{124}, β_{156}) (See table 1) [24, 25]. They are then added to calculate the total polarization $\mathbf{P=P_1+P_2}$:

$$\mathbf{P_1} = 2e_{14} \begin{pmatrix} \epsilon_{yz} \\ \epsilon_{xz} \\ \epsilon_{xy} \end{pmatrix} \qquad (1)$$

$$\mathbf{P_2} = B_{114} \begin{pmatrix} \epsilon_{xx}\epsilon_{yz} \\ \epsilon_{yy}\epsilon_{xz} \\ \epsilon_{zz}\epsilon_{xy} \end{pmatrix} + B_{124} \begin{pmatrix} \epsilon_{yz}(\epsilon_{yy} + \varepsilon_{zz}) \\ \epsilon_{xz}(\epsilon_{zz} + \varepsilon_{xx}) \\ \epsilon_{xy}(\epsilon_{xx} + \varepsilon_{yy}) \end{pmatrix} + B_{156} \begin{pmatrix} \epsilon_{xz}\epsilon_{xy} \\ \epsilon_{yz}\epsilon_{xy} \\ \epsilon_{yz}\epsilon_{xz} \end{pmatrix} \qquad (2)$$

The divergence of the total polarization $\mathbf{P}$ is calculated over a rectangular mesh using a finite difference approach to calculate total charge density $\rho(\mathbf{r})$:

$$\rho(\mathbf{r}) = -\nabla.\mathbf{P} \qquad (3)$$

Finally, the Poisson equation (4) is solved to calculate the piezoelectric potential $V_p(\mathbf{r})$, taking into account the position dependence of the static dielectric constant, $\varepsilon_s(\mathbf{r})$. The value of the dielectric constant for vacuum ε_0 is 8.85x10-12F/m. For InGaAs and GaAs materials, we used the relative dielectric constant values of $14.0\varepsilon_0$ and $12.84\varepsilon_0$, respectively.

$$\rho(\mathbf{r}) = \varepsilon_0 \nabla.[\varepsilon_s(\mathbf{r}) \nabla V_p(\mathbf{r})] \qquad (4)$$

5.3. Quadrupole Nature of the Piezoelectric Potentials

Figure 5.1(a) shows the first order (solid line with square), the second order (dashed line), and the sum of the first and second order (solid line with circle) piezoelectric potentials along the [001] direction through the center of the quantum dot molecule. It is evident that the net piezoelectric potential is nonzero inside the quantum dot and penetrates into the surrounding GaAs buffer. The reason for the nonzero net potential inside the quantum dot is that the quadratic (second order –> dashed line) component of the potential is significantly reduced for alloyed quantum dots ($In_{0.5}Ga_{0.5}As$) due to the following reasons: (1) Increasing the „Ga" concentration reduces the diagonal strain components that determine the quadratic component.

(2) The polarization constant B_{124}, which comprises a major portion of the quadratic component is reduced in magnitude. The linear (first order –> solid line with square) component, on the other hand, increases mainly due to the large increase of e_{14}. The reduced quadratic component cannot cancel the effect of the already enhanced linear component, and hence the interior of the quantum dot will have a nonzero potential largely dominated by the linear component (see the solid line with circle). Outside of the quantum dot, the quadratic component is negligible, and only the linear component is dominant. As a result, the net piezoelectric effect inside and at the interfaces of the quantum dots is no longer found to be negligible.

Polarization Constant	Type of Component	GaAs (C/m^2)	InAs (C/m^2)	In$_{0.5}$Ga$_{0.5}$As (C/m^2)
e_{14}	Linear (Experiment)	-0.16	-0.045	-0.1025
e_{14}	Linear (Calculated)	-0.23	-0.115	-0.1725
B_{114}	Quadratic (Calculated)	-0.439	-0.531	-0.485
B_{124}	Quadratic (Calculated)	-3.765	-4.076	-3.9205
B_{156}	Quadratic (Calculated)	-0.492	-0.12	-0.306

Table 1: Polarization constants for calculation of piezoelectric potential from reference [24]. The values for In$_{0.5}$Ga$_{0.5}$As are obtained by linear interpolation between GaAs and InAs.
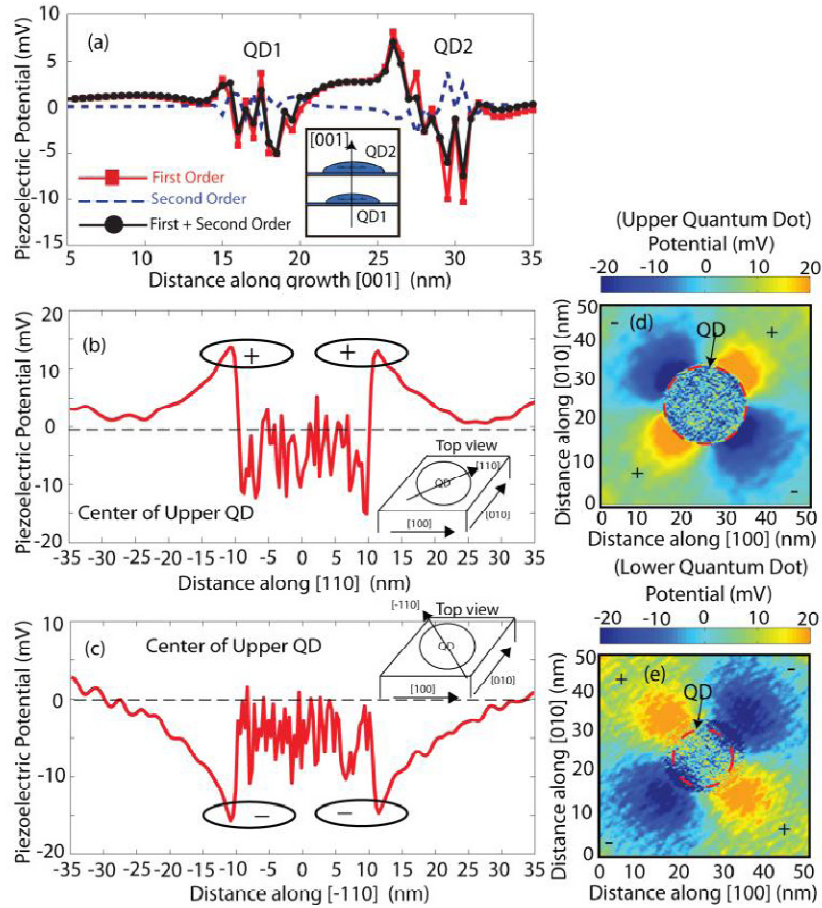
Figure 5.1: **(a)** The first order (line with the box), second order (dashed line) and the sum of first and second order (line with the circle) piezoelectric potential are shown through the center of the quantum dot along the [001] growth direction. The net potential is clearly nonzero inside the quantum dots, at the interfaces of the quantum dot and in the surrounding buffer. The second order piezoelectric effect is weak and cannot cancel the first order effect inside the quantum dot. **(b, c)** Piezoelectric potential plotted through the center of the upper quantum dot in the [110] and [$\bar{1}$10] directions. The origin of the x-axis is taken at the center of the quantum dot. The quadrupole nature of the potentials is clearly evident: the potential is positive at the interface of the quantum dot and buffer along the [110] direction, whereas it is negative at the interface of the quantum dot and buffer along the [$\bar{1}$10] direction. The random nature of the potential inside the quantum dot region is a result of the random alloy configuration of the $In_{0.5}Ga_{0.5}As$ quantum dot material. The quadrupole nature of the piezoelectric potential along diagonal directions strongly affects the splitting and orientation of the electron P-states, which are aligned along these directions due to atomistic asymmetry. **(d, e)** The two dimensional (xy) contour plots of the net piezoelectric potential at the base of the lower and upper quantum dots are shown as a function of distance along the [100]- and [010]-axis. The quadrupole nature of the potential is clearly evident from the plots. Furthermore, the potential is long ranged and penetrates deep inside the GaAs buffer.

Figures 5.1(b,c) show the net piezoelectric potential along the diagonal [110] and [$\bar{1}$10]directions through the center of the upper quantum dot. Figure 5.1(d, e) show the two dimensional contour plots of the net piezoelectric potentials about 1nm above the base of the lower and upper quantum dots. The quadrupole nature of the net piezoelectric potentials along the diagonal directions is clearly evident. The piezoelectric potentials along the [110] and [$\bar{1}$10] directions are large at the interfaces, where strain is large and penetrates deep into the GaAs buffer [26, 27]. A large GaAs buffer is therefore not only required along the [001] direction, but also in the plane of the quantum dot to fully capture the effect of the piezoelectric potential reaching 25-30nm deep into the GaAs buffer. The wide extension of the piezoelectric fields in the lateral plane also implies that the quantum dots that are closer than ~30 nm will interact with each other through the piezoelectric potentials.

Past studies [26-29] have shown that the quadrupole nature of the piezoelectric effect significantly changes the splitting and orientation of electron P-states, which are already oriented along diagonal directions due to atomistic interface and strain asymmetry. In figure 4.1(b), the optically active states in the experimental spectrum are identified as excited states (E_3 and E_4) in the range of applied bias. The next paragraph shows that considering piezoelectric effects is indeed critical in reproducing the experimental excitonic spectrum.

5.4 Quantitative Explanation of 'One' vs. 'Two' Anti-Crossings

Figure 5.2 presents a quantitative explanation of the presence of 'one' and 'two' anti-crossings. It shows a flow diagram in two directions: (Flow to right) First six electron states without piezoelectricity and without electrical field   with piezoelectricity but without electrical field   with piezoelectricity and with electric field of 15kV/cm. (Flow to left) First six electron states without piezoelectricity and without electrical field   without piezoelectricity and with electric field of 15kV/cm. It is critical to investigate the arrangement of the electron states at 15kV/cm to understand the resonance behavior at higher electric field values.

Since the first hole state remains in the upper quantum dot throughout the sweeping process of the electrical field, it is not included in figure 5.2. Piezoelectricity shifts the ground electron state E_1(U-S) only by a very small value of 0.59meV. The major contribution towards the shifting of the ground electron state comes from the externally applied bias. Hence, the total shift in this state in either direction is approximately the same: Left=15.09meV, Right=15.01+0.59=15.6meV. The most significant effect of the piezoelectric effect is found to be on the E_5(L-P_x) and E_6(L-P_y) electron states. These states are not only shifted by a larger magnitude, but also their relative order is changed.

Similar behavior has been observed in previous studies for a single quantum dot [25-27, 29], in which a strong piezoelectric effect has been shown to flip the order of the electron P-states. Here, the piezoelectric effect induces a shift of 0.7meV and 3.2meV in E_5(L-P_x) and E_6(L-P_y) respectively, followed by an additional electric field induced shift of 7.7meV and 11.5meV respectively. This total shift of 3.2+11.5=14.7meV causes E_6(L-P_y) to become E_2(L-P_y) at 15kV/cm, which is below E_3(U-S) on the same energy scale. A further increase of the electrical field beyond 15kV/cm will shift E_3(U-S) to higher energies and E_4(L-P_x) to lower energies. This will result in a resonant coupling of these two states with one anti-crossing (E_3 E_4) in the emission spectra. Going in the left direction according to figure 5.2 with no piezoelectricity included, there will be no additional shift of 3.2meV and 0.7meV in the lower quantum dot P-states. Mere electric field induced shifts of 10.02meV and 10.11meV are not sufficient enough to push either of the two excited states below E_2(U-S). This results in the observation of two anti-crossings (E_2 E_3 E_4).

L-S = Lower QD S-sate   U-S = Upper QD S-state P_x = P along [110] P_y = P along [-110]
L-P_i = Lower QD P_i-state U-P_i = Upper QD P_i-state

Piezoelectric induced flipping

Energy (eV)

1.391
1.386
1.381
1.376
1.371
1.366
1.361
1.356

L-P_y
L-P_x

Δ =10.11meV

L-P_y
L-P_x
Anticross

Δ =10.02meV

U-S

Δ =15.09meV

L-S

Δ =7.9meV

L-P_y
L-P_x

Δ =0.7meV   L-P_x
Δ =3.2meV
L-P_y

Δ =7.7meV

U-P_y
U-P_x

Δ =0.3meV   U-P_y
Δ =0.4meV   U-P_x

Δ =11.5meV

U-S
L-P_y
Anticross

L-S   Δ =0.03meV
L-S

Δ =15.01meV

Δ =8.1meV

U-S   Δ =0.59meV
U-S

L-P_x

L-S

No Piezoelectricity
With F = 15kV/cm

No Piezoelectricity
No Electrical Field

With Piezoelectricity
No Electrical Field

With Piezoelectricity
With F = 15kV/cm

Dynamics of Lowest Six Electron States in Conduction Band

Figure 5.2: Flow diagram showing the arrangement and position of the first six electron states in the conduction band of the quantum dot molecule. Piezoelectric effects reorder the P-states in the lower quantum dot and play a critical role in determining the resonances occurring at higher electric field strengths.

6. CONCLUSIONS

In this work, we presented a detailed systematic atomistic tight binding study of an experimental single quantum dot molecule geometry, taking into account long range strain, atomistic interface asymmetry, and both linear and the quadratic piezoelectric effects. The quantum dot molecule energy states are composed of individual single quantum dot states, which can interact with each other depending on their energetic alignment. The external electrical field enables tuning of the relative alignment of molecular and atomic states, which has been observed in experimental spectroscopy data [12]. Our calculations quantitatively reproduce the experimental spectra. The interband transition strengths are calculated to compare the relative intensities of the excitonic emissions and to characterize them as either optically active or inactive states. The calculated transition strengths closely follow the experimentally measured intensities and identify the excited electron (P-states) states as the optically active states in the range of the applied electrical field. The close quantitative agreement of our theoretical calculations with the experimental data [12] allows us to gain significant physical insight of the investigated quantum dot molecule. We sweep the electrical field from zero to 21kV/cm and provide a spectroscopic mapping of the lower quantum dot electron states and the upper quantum dot hole excited states. Analysis of the observed sequence of anti-crossings provides a technique to precisely probe the energy states of one quantum dot with the help of the energy states of the neighboring quantum dot. The direction of the applied electrical field determines the quantum dot whose electron/hole electronic states will be probed by increasing the electrical field magnitude. This technique can be used to „reverse engineer" the geometry of the quantum dot molecule from the experimentally measured optical spectrum.

The strain and piezoelectric fields are both found to be long range effects. This imposes the need of a large simulation domain size consisting of about 15 million atoms in the strain domain and about 9 million atoms in the electronic domain. Our calculations include both first order and second order piezoelectric fields. The quadrupole nature of the net piezoelectric effect along [110] and [$\bar{1}$10] directions significantly affects the splitting and orientation of the excited electron states.

The NEMO 3-D based atomistic study shows that the net piezoelectric effect is critical in reproducing the experimentally observed optical transitions. Continuum methods such as the effective mass model and k•p method do not take into account the atomistic nature of the InGaAs quantum dots and thus cannot correctly incorporate the strain and piezoelectric fields.

Major parts of the work presented in this thesis are currently under review for publication in ACS Nano.

Quantitative Excited State Spectroscopy of a Single InGaAs Quantum Dot Molecule through Multi-million Atom Electronic Structure Calculations

Muhammad Usman, Yui Hong Matthias Tan, et al.   http://arxiv.org/abs/1008.3127

LIST OF REFERENCES

[1] P. Michler, "Single Quantum Dot", Springer, Berlin, 2003

[2] D. Bimberg, "Semiconductor Nanostructures", Springer Berlin, 2008; D. Bimberg, M. Grundmann, and N. N. Ledentsov, "Quantum Dot Heterostructures", John Wiley & Sons, Chichester, 1999;

[3] N. H. Bondeo, J. Erland, D. Gammon, D. Park, D. S. Katzer and D. G. Steel, Science 282, 1473, 1998

[4] Xiaoqin Li et al., Science 301, 809, 2003

[5] D. Loss and D. P. DiVincenzo, Phys. Rev. A 57, 120, 1998.

[6] W. G. van der Wiel, S. D. Franceschi, J. M. Elzerman, T. Fujisawa, S. Tarucha, and L. P. Kouwenhoven, Rev. Mod. Phys. 75, 1, 2003

[7] O. Gywat, G. Burkard, and D. Loss, Superlattices and Microstrctures 31, 127, 2002.

[8] X. Q. Li and Y. Arakawa, Phys. Rev. A 63, 012302, 2000.

[9] B. W. Lovett, J. H. Reina, A. Nazir, and G. A. Briggs, Phys. Rev. B 68, 205319, 2003.

[10] T. H. Oosterkamp et al., Nature 395, 873, 1998.

[11] M. Bayer et al., Science 291, 451, 2001.

[12] H. J. Krenner, M. Sabathil, E.C. Clark, A. Kress, D. Schuh, M. Bichler, G. Abstrieter, and J.J. Finely, "Direct observation of controlled coupling in an individual quantum dot molecule," Phys. Rev. Lett. 94, 057402 (2005)

[13] G. Klimeck, S. Ahmed, H. Bae, N. Kharche, R. Rahman, S. Clark, B. Haley, S. Lee, M. Naumov, H. Ryu, F. Saied, M. Prada, M. Korkusinski, and T.B. Boykin, "Atomistic simulation of realistically sized Nanodevices using NEMO 3-D: Part I – Models and Benchmarks," (INVITED) Special issue on NanoElectronic device modeling in *IEEE* Transactions Electron Devices, vol. 54, no. 9, pp. 2079-2089, Sep. 2007

[14] G. Klimeck, S. Ahmed, N. Kharche, M. Korkusinski, M. Usman, M. Prada, and T.B. Boykin, "Atomistic simulation of realistically sized Nanodevices using NEMO 3-D: Part II – Applications," (INVITED) Special issue on NanoElectronic device modeling in *IEEE* Transactions Electron Devices, vol. 54, no. 9, pp. 2079-2089, Sep. 2007

[15] G. Klimeck, F. Oyafuso, T.B. Boykin, R.C. Bowen, and P. V. Allmen, "Development of a nanoelectronic 3-D (NEMO 3-D) simulator for multimillion atom simulations and its application to alloyed quantum dots," (INVITED) Computer Modeling in engineering and Science (CMES), vol. 3 no.5, pp. 601-642 (2002)

[16] M. Usman, H. Ryu, I. Woo, D.S. Ebert, and G. Klimeck, "Moving towards Nano-TCAD through multi-million atom quantum dot simulations matching experimental data", *IEEE* Trans. on Nanotechnology, vol. 8, No. 3, May 2009

[17] T.B. Boykin, G. Klimeck, R.C. Bowen, and F. Oyafuso, "Diagonal parameter shifts due to nearest-neighbor displacements in empirical tight binding theory," Physical rev. B 66, 125207 (2002)

[18] P. Keating, "Effect of invariance requirements on the elastic strain energy of crystal with application to diamond structure," Physical Rev. 145, no. 2, pp.737, May 1966.

[19] R. Rahman, C.J. Wellard, F.R. Bradbury, M. Prada, J.H. Cole, G. Klimeck, and L.C.L. Hollenberg, "High precision quantum control of single donor spins in Si," Phys. Rev. Lett. 99, 036403 (2007)

[20] G.P. Lansbergen, R. Rahman, C.J. Wellard, P.E. Rutten, J. Caro, N.cCollaert, S. Biesemans, I. Woo, G. Klimeck, L.C.L. Hollenberg, and S. Rogge, "Gate induced quantum confinement transition of a single dopant atom in a Si FinFET," Nature Physics, vol. 4, p.656 (2008)

[21] N. Kharche, M. Prada, T.B. Boykin, and G. Klimeck, "Valley-splitting in strained Silicon quantum wells modeled with 2 degree miscut, step disorder and alloy disorder," Appl. Phys. Lett. 90, 092109 (2007)

[22] Muhammad Usman, Shaikh Ahmed, and Gerhard Klimeck, "Atomistic tight binding study of strain-reduced confinement potentials in identical and non-identical InAs/GaAs vertically stacked quantum dots," in proc. of 8th IEEE NANO Arlington TX, August 2008, pp. 541-544.

[23] G. Bester, X. Wu, D. Vanderbilt, and A. Zunger, "Importance of second-order piezoelectric effects in zinc-blende semiconductors," Phys. Rev. Lett. 96, 187602 (2006)

[24] G. Bester, A. Zunger, X. Wu, and D. Vanderbilt, "Effects of linear and nonlinear piezoelectricity on the electronic properties of InAs/GaAs quantum dots," Physical Rev. B 74, 081305(R) (2006)

[25] G. Bester and A. Zunger, "Cylindrically shaped zinc-blende semiconductor quantum dots do not have cylindrical symmetry: Atomistic symmetry, atomic relaxation, and piezoelectric effects," Physical Rev. B 71, 045318 (2005)

[26] S. Islam, S. Sundaresan, and S. Ahmed, "Geometry dependence of the internal fields and its impact on the electronic structure in self-assembled InAs/GaAs quantum dots," *IEEE* Trans. on Nanotechnology (under review)

[27] Shaikh Ahmed, Muhammad Usman, N. Kharche, Andrei Schliwa, and Gerhard Klimeck, "Atomistic simulation of non-degeneracy and optical polarization anisotropy in pyramidal quantum dots," in proc. of IEEE NEMs, Bangkok Thailand, January 16-19, 2007, pp.937-942

[28] A. Schliwa, M. Winkelnkemper, and D. Bimberg, "Few-particle energies versus geometry and composition of InGaAs/GaAs self-organized quantum dots," Physical Rev. B 79, 075443 (2009)

[29] A. Schliwa, M. Winkelnkemper, and D. Bimberg, "Impact of size, shape, and composition on piezoelectric effects and electronic properties of In(Ga)As/GaAs quantum dots," Physical Rev B 76, 205324 (2007)

[30] L.R.C. Fonseca, J.L. Jimenez, and J.P. Leburton, "Electronic coupling in InAs/GaAs self-assembled stacked double-quantum-dot systems," Physical Rev. B 58, 9955 (1998-I)

[31] Olga L. Lazarenkova, P. von Allmen, F. Oyafuso, S. Lee, and G. Klimeck, "Effect of anharmonicity of the strain energy on band offsets in semiconductor nanostructures," Appl. Phys. Lett. 85, 4193 (2004)

[32] Muhammad Usman, Hoon Ryu, Sunhee Lee, Yui H. Matthias Tan, and Gerhard Klimeck, "Quantum confined stark shift and ground state optical transition rate in [100] laterally biased InAs/GaAs quantum dots" IEEE proceedings of 13th International workshop on computational electronics IWCE China, May 27-29 (2009)

[33] P.W. Fry et al., Phys. Rev. Lett. 84, 733 (2000)

[34] M.F. Doty, J.I. Climente, A. Greilich, M. Yakes, A.S. Bracher, and D. Gommon, "Hole spin mixing in InAs quantum dot molecule," Physical Rev. B 81, 035308 (2010)

[35] D. Litvinov, H. Blank, R. Schneider, D. Gerthsen, T. Vallaitis, J. Leuthold, T. Passow, A. Grau, H. Kalt, C. Klingshirn, and M. Hetterich, "Influence of InGaAs cap layers with different In concentration on the properties of InGaAs quantum dots," Journal of Appl. Physics 103, 083532 (2008)

[36] Marek Korkusinski and Gerhard Klimeck, "Atomistic simulations of long-range strain and spatial asymmetry molecular states of seven quantum dots", Journal of Physics: Conference Series, Vol. 38, pg. 75-78 (2006)

[37] M. Scheibner, M. Yakes, A.S. Bracker, I.V. Ponomarev, M.F. Doty, C.S. Hellberg, L.J. Whitman, T.L. Reinecke, and D. Gammon, "Optically mapping the electronic structure of coupled quantum dots", Nature Physics, Vol. 4 pp. 291-295 (2008)

[38] Shaikh Ahmed, Neerav Kharche, Rajib Rahman, Muhammad Usman, Sunhee Lee, Hoon Ryu, Hansang Bae, Steve Clark, Benjamin Haley, Maxim Naumov, Faisal Saied, Marek Korkusinski, Rick Kennel, Michael McLennan, Timothy B. Boykin, Gerhard Klimeck, "Multimillion Atom Simulations with NEMO 3-D" published in Springer Encyclopedia for Complexity, 2008 (Full Paper at arXiv:0901.1890v1)

[39] Timothy B. Boykin and P. Vogl, "Dielectric response of molecules in empirical tight binding theory", Phys. Rev. B 65, 035202 (2001)

[40] Timothy B. Boykin, R. Chris Bowen, and Gerhard Klimeck, "Electromagnetic coupling and gauge invariance in the empirical tight binding theory", Phys. Rev B 63, 245314 (2001)

[41] M. Graf and P. Vogl, Phys. Rev. B 51, 4940 (1995)

[42] S. Lee, J. Kim, L. Jönsson, J. W. Wilkins, G. Bryant, and G. Klimeck, "Many-body levels of multiply charged and laser-excited InAs nanocrystals modeled by empirical tight binding," *Phys. Rev. B, Condens. Matter*, vol. 66, p. 235 307, 2002.

[43] T. B. Boykin, G. Klimeck, R. C. Bowen, and F. Oyafuso, "Diagonal parameter shifts due to nearest-neighbor displacements in empirical tight-binding theory," *Phys. Rev. B, Condens. Matter*, vol. 66, no. 12, p. 125 207, Sep. 2002.

[44] G. Klimeck, F. Oyafuso, T. Boykin, R. Bowen, and P. von Allmen, "Development of a nanoelectronic 3-D (NEMO 3-D) simulator for multimillion atom simulations and its application to alloyed quantum dots," *Comput. Model. Eng. Sci.*, vol. 3, p. 601, 2002.

[45] G. Klimeck, R. C. Bowen, T. B. Boykin, C. Salazar-Lazaro, T. A. Cwik, and A. Stoica, "Si tight-binding parameters from genetic algorithm fitting," *Superlattices Microstruct.*, vol. 27, no. 2/3, pp. 77–88, Mar. 2000.
[46] K. Eberl, "Quantum Dot lasers", Physics World, Sept. 1997, p. 47-50

[47] D. Mowbray, M. Skolnick, " New physics and devices based on self-assembled semiconductor quantum dots", J. Phys. D: Appl. Phys. 38 (2005)

[48] S. Li, Xia, J. Bai, "Quantum-confined Stark effects of InAs/GaAs self-assembled quantum dot", Journal of Applied Physics, Vol. 88, Issue 12, pp. 7171-7174 (2000)

[49] K. L. Janssens, B Partoens, F. M. Peeters, "Stark shift in single and vertically coupled type-I and type-II quantum dots", Physical Review B, Vol. 65, 233301, 2002

[50] S. Raymond, J.P. Reynolds, J.L. Merz, S. Fafard, Y. Feng, S. Charbonneau, "Asymmetric Stark shift in $Al_xIn_{1-x}As/Al_yGa_{1-y}As$ self-assembled dots", Physical Review B, Vol. 58, Nr. 20, 1998